The Astronomical Journal, 139:2097–2129, 2010 June doi:10.1088/0004-6256/139/6/2097

DETAILED DECOMPOSITION OF GALAXY IMAGES. II. BEYOND AXISYMMETRIC MODELS

Chien Y. Peng[1], Luis C. Ho[2], Chris D. Impey[3], and Hans-Walter Rix[4]
[1] Herzberg Institute of Astrophysics, National Research Council of Canada, 5071 West Saanich Road, Victoria, British Columbia V9E 2E7, Canada; cyp@nrc-cnrc.gc.ca
[2] The Observatories of the Carnegie Institution for Science, 813 Santa Barbara Street, Pasadena, CA 91101, USA; lho@obs.carnegiescience.edu
[3] Steward Observatory, University of Arizona, 933 North Cherry Avenue, Tucson, AZ 85721, USA; cimpey@as.arizona.edu
[4] Max-Planck-Institut für Astronomie, Koenigstuhl 17, Heidelberg, D-69117, Germany; rix@mpia-hd.mpg.de
Received 2009 October 1; accepted 2009 December 29; published 2010 April 13

ABSTRACT

We present a two-dimensional (2D) fitting algorithm (Galfit, ver. 3) with new capabilities to study the structural components of galaxies and other astronomical objects in digital images. Our technique improves on previous 2D fitting algorithms by allowing for irregular, curved, logarithmic and power-law spirals, ring, and truncated shapes in otherwise traditional parametric functions like the Sérsic, Moffat, King, Ferrer, etc., profiles. One can mix and match these new shape features freely, with or without constraints, and apply them to an arbitrary number of model components of numerous profile types, so as to produce realistic-looking galaxy model images. Yet, despite the potential for extreme complexity, the meaning of the key parameters like the Sérsic index, effective radius, or luminosity remains intuitive and essentially unchanged. The new features have an interesting potential for use to quantify the degree of asymmetry of galaxies, to quantify low surface brightness tidal features beneath and beyond luminous galaxies, to allow more realistic decompositions of galaxy subcomponents in the presence of strong rings and spiral arms, and to enable ways to gauge the uncertainties when decomposing galaxy subcomponents. We illustrate these new features by way of several case studies that display various levels of complexity.

Key words: galaxies: bulges – galaxies: fundamental parameters – galaxies: structure – techniques: image processing – techniques: photometric

Online-only material: color figures

1. INTRODUCTION

Images of astronomical objects store a wealth of information that encodes the physical conditions and fossil records of their evolution. Over the past decade, the ability of optical/near-infrared telescopes to resolve objects improved by a factor of 10, and to detect faint surface brightnesses by at least 2 orders of magnitude. These advances now enable the study of highly intricate details on subarcsecond scales (e.g., nuclear star cluster, spiral structure, bars, inner ring, profile cusps, etc.) and extremely faint outer regions of galaxies. Moreover, new integral-field imaging capabilities blur the traditional boundary of obtaining, analyzing, and interpreting imaging and spectroscopic data. Faced with the convergence in volume, quality, and multiwavelength data sets like never before, one of the main challenges toward making full use of the investments is developing sophisticated ways to extract information from the data to facilitate new science.

1.1. Parametric and Non-parametric Analysis

Analyzing astronomical images is challenging because of the diversity in object sizes and shapes, and nowhere is it more difficult than for galaxies. Since the early era of photographic plates, one of the key methods for studying the light distribution of galaxies is to model it by using analytic functions—a technique known as parametric fitting. This technique was first applied to galaxies by de Vaucouleurs (1948) who showed that the light distribution of elliptical galaxies tended to follow a power-law form of $\exp(-r^{1/4})$. Subsequently, one of the breakthroughs in our understanding of galaxy structure and evolution came when Freeman (1970) showed that dynamically "hot" stars in galaxies make up spheroidal bulges having a de Vaucouleurs light profile, whereas "cold" stellar components make up the more flattened, rotationally supported, exponential disk region.

From that simple beginning, parametric fitting has been the mainstay for galaxy imaging studies, and expanding into many applications whenever the science calls for detailed and rigorous analysis. Among some of the examples, past investigations delved into the structural parameters of disk galaxies (e.g., de Jong 1996), the Tully–Fisher relation (e.g., Tully & Fisher 1977; Hinz et al. 2003; Bedregal et al. 2006), the evolution of disky galaxies (Simard et al. 2002; Ravindranath et al. 2004; Barden et al. 2005), the cosmic evolution of galaxy morphology (e.g., Lilly et al. 1998; Marleau & Simard 1998; Hathi et al. 2009) in both ground-based surveys and Hubble (Ultra-)Deep Fields (Williams et al. 1996; Beckwith et al. 2006), the morphological transformation of galaxies in cluster environments (e.g., Dressler 1980), the fundamental plane of spheroids (Djorgovski & Davis 1987; Dressler et al. 1987; Bender et al. 1992), the red sequence of galaxies (Bell et al. 2004a, 2004b; Faber et al. 2007), morphological dissimilarities between spheroidal galaxies and ellipticals (Kormendy 1985, 1987), the central structure of early-type galaxies (Kormendy 1985; Lauer et al. 1995, 2007; Faber et al. 1997; Ferrarese et al. 2006a, 2006b) and implications for the formation of massive black holes (Ravindranath et al. 2002; Kormendy & Bender 2009), black hole versus bulge relations (Kormendy & Richstone 1995) and their evolution (Rix et al. 2001; Peng et al. 2006a, 2006b), the "extra light" due to gas dissipation in galaxy centers (Kormendy 1999; Cote et al. 2006, 2007; Kormendy et al. 2009; Hopkins et al. 2008, 2009), quasar host galaxies (e.g., Hutchings et al. 1984; McLeod & Rieke 1994; McLure et al. 2000; Jahnke et al. 2004; Sánchez et al.

2004; Kim et al. 2008b), gravitational lensing of quasar host galaxies (Rix et al. 2001; Peng et al. 2006b), and the clustering of dark matter through weak lensing (e.g., Heymans et al. 2006, 2008).

Since the original development of galaxy fitting nearly 70 years ago, where the analysis was performed on one-dimensional (1D) surface brightness profiles (see also Kormendy 1977; Burstein 1979; Boroson 1981; Kent 1985; Andredakis & Sanders 1994; MacArthur et al. 2003), newer techniques have emerged to directly analyze two-dimensional (2D) images (e.g., Shaw & Gilmore 1989; McLeod & Rieke 1994; Byun & Freeman 1995; de Jong 1996; Moriondo et al. 1998; Simard 1998; Ratnatunga et al. 1999; Wadadekar et al. 1999; Simard et al. 2002; de Souza et al. 2004; Laurikainen et al. 2004 ; Gadotti 2008). The benefit of performing 2D image analysis is to potentially make full use of all spatial information and to properly account for image smearing by the point-spread function (PSF).

Even though 2D analysis can be quite sophisticated, there are legitimate questions about whether it is more beneficial than 1D for profile analysis. Proponents of the 1D technique are skeptical that perfect ellipsoid models are suitable to use for galaxies that show isophotal twists, or that are non-elliptical in shape. They note that not only is 1D analysis more appealing because it is more straightforward to implement, but also the surface brightness profiles serve as visual confirmation about the reality of fitting multiple-component models.

However, beneath the apparent simplicity there are a number of important subtleties to weigh. For instance, the decision about how to extract 1D profiles is often not unique, nor are there strong reasons to prefer major or minor axis profiles, or a profile along some arc traced by spiral arms or isophote twists that result from the superposition of multiple components oriented at different angles. When symmetry is broken, it is also unclear that there is an optimal or unique way to extract a 1D profile, such as in irregular galaxies, overlapping galaxies, and galaxies with double nuclei. Another factor to consider is that the process of extracting 1D profiles reduces spatial information content: in many situations, a bulge, disk, and bar can all have different axis ratios, position angles (P.A.s), and profiles that help to break model degeneracies, but this information is lost when the data are collapsed into 1D. Lastly, for compact galaxies, 1D profile fitting cannot properly correct for image smearing by the PSF because 1D profile convolution is not mathematically equivalent to convolution in a 2D image. While some of the above concerns also affect 2D analysis (i.e., irregular galaxies), most others benefit from treatment using 2D techniques. When it comes to judging which models are more plausible, there are few diagnostics more discerning than a moment's glance at 2D models and residual images; a good fit in 2D always means that 1D profiles are necessarily a good fit. Proponents of 2D analysis therefore believe that the benefits outweigh the drawbacks. Moreover, many drawbacks can be mitigated by breaking free from axisymmetry in 2D analysis, which we aim to show in this study.

In the box of tools for morphology analysis, a complimentary approach is non-parametric analysis. While we do not use non-parametric methods in this study, it is useful to understand the conceptual differences between the two approaches. We thus provide a brief overview. In contrast to function fitting, the non-parametric approach does not involve deciding what functional form to use or how many. One method is to decompose an image into "shapelets" or "wavelets" (e.g., Refregier 2003; Massey et al. 2004), which is analogous to taking a 2D Fourier transform of an image using mathematically orthogonal basis functions. The main conceptual difference with parametric fitting is that the shapelet basis functions do not represent physical subcomponents of a galaxy. Moreover, the power spectrum of the basis functions is quite useful for diagnosing the degree of galaxy distortions. There are also other non-parametric techniques (e.g., Abraham et al. 1994; Rudnick & Rix 1998; Conselice et al. 2000; Lotz et al. 2004). To measure concentration non-parametrically, one way is to compare fluxes within apertures of different radii; whereas to measure asymmetry one can rotate an image by 180° and subtract it from the original image and measure the residuals (e.g., Abraham et al. 1994; Conselice et al. 2000). Toward the same goals, two studies, Abraham et al. (2003) and Lotz et al. (2004), introduce the Gini index to measure the concentration of a galaxy by comparing the relative distribution of pixel flux values within a certain area. Lotz et al. (2004) also introduce a method for measuring asymmetry through the M_{20} parameter, which is the second-order moment of the brightest 20% of a galaxy's flux.

The application of non-parametric analysis has mostly been to quantify galaxy mergers (e.g., Conselice et al. 2003; Lotz et al. 2008). These techniques are generally much simpler to implement than parametric fitting and have a strong virtue that no assumptions are made about the galaxy profiles and shapes. The trade-off is that the techniques often do not deal with image smearing by the PSF and different sensitivity thresholds between different surveys. Consequently, one has to take particular care to compare compact with extended objects, measured in different apertures, or measured from images of different surface brightness depths (Lisker 2008). One also should guard against contamination by intervening galaxies or stars because the techniques do not have a rigorous way to separate overlapping objects. For separating objects, extracting structural components of a galaxy, and extrapolating galaxy wings well into the background noise, there are few, if any, alternatives to parametric analysis that are more rigorous.

When comparing the merits of non-parametric and parametric analysis, the idea of ellipsoid models in parametric analysis is sometimes considered to be a weakness, because galaxies, after all, are not perfect ellipses in projection. However, it is worth pointing out that the notion of there being a *global average* size inherently implies comparison against some kind of approximate shape. Indeed, even in non-parametric techniques, to measure a size in a 2D image, one assumes a basic shape either explicitly (through using aperture photometry) or implicitly (through calculating flux moments, which requires a center to be defined). An ellipsoid is one of the simplest and most natural low-order shapes against which all galaxies can be compared, especially for measuring an average size. This notion is useful: deviations from the basic ellipsoid shape can then be considered as higher order modifications, even for highly irregular galaxies.

Nevertheless, there are many situations where it is desirable to use models that deviate from ellipsoid shapes. Contrary to the common practice, there are numerous ways to break from axisymmetry. However, the harder challenge is to devise a scheme that is intuitive to grasp and well motivated. Breaking free from axisymmetry allows for other interesting science applications, including a promising new way to quantify asymmetry.

1.2. The Next Generation of Parametric Imaging Fitting

In this study, we present, as a proof of concept, new capabilities in 2D image fitting that progress beyond the limitations of traditional parametric fitting models. One key aspect of our approach is to first identify a minimum basis set of features that spans the range of galaxy morphologies and shapes. From experience, we determine those four "basic elements" to be bending, Fourier, coordinate rotation, and truncation modes. Second, one of the main reasons why parametric fitting is useful is that the profile parameters are intuitive to grasp (e.g., concentration index, effective radius, total luminosity, etc.). Therefore, another key requirement is that the traditional profile parameters must retain their original, intuitive, meaning even under detailed shape refinements, and even under such extreme cases as irregular galaxies. This can be accomplished if the basic premise starts with the traditional ellipsoid function, on top of which one can add perturbations, rotations, irregularities, and curvature. This is possible because of the fact that simple ellipsoid fits are a reasonable way to quantify global average properties, and other details can be considered to be higher order perturbations that may be of other practical interest.

As we attempt to demonstrate, combining just the four basic morphology elements can quickly yield a dizzying array of possibilities for fitting galaxies. The end result can look highly "realistic." Indeed, it is now possible to fit many spiral galaxies, asymmetric tidal features, irregular galaxies, ring galaxies, dust lanes, truncated galaxies, arcs, among others (though, certainly, there are limitations). However, it is important to realize that "being possible" often does not mean "being necessary" or "being practical." Necessity ought to be judged in the scientific context of whether it is worth the extra effort to obtain diminishing returns. For instance, to measure total galaxy luminosity, it is often unnecessary to fit high-order Fourier modes or spiral rotations. For many science studies interested in global parameterization, often a single ellipsoid component would suffice. It is therefore important to always let the science determine what kind of analysis is required, rather than to use the new capabilities in the absence of a clearly defined goal. Having provided some foregoing disclaimers, some of the key scientific reasons motivating the new capabilities are to: (1) quantify global asymmetry or substructure asymmetry; (2) quantify bending modes for weak-lensing applications, or fit arcs in the image plane for strong gravitational lenses; (3) obtain more accurate substructure decomposition in the presence of bars, spirals, rings, etc.; (4) obtain more accurate global photometry; (5) quantify profile deviation in inner or outer regions of a galaxy, such as disk truncations, deviations from a Sérsic function, etc.; (6) Extract parametric information to the limits imposed by resolution, signal-to-noise ratio (S/N), and other small-scale fluctuations; and (7) quantify model-dependent errors in the decomposition.

We thus begin by giving an overview of the GALFIT software (Section 2). Then, we introduce the radial profile functions that one can use (Section 3), and illustrate how symmetric and asymmetric shapes can be generated by modifying the coordinate system in Section 4. Next, we introduce a new capability that allows for radial profile truncation (Section 5). Enabling all the capabilities may result in extremely complex galaxy shapes, the interpretation of which may give concerns to those new to the analysis. Therefore, we discuss the interpretations and model degeneracies of the parameters in Section 6. We then apply these new features to real galaxies in Section 7, followed by concluding remarks (Section 8).

2. THE 2D FITTING PROGRAM GALFIT

This study builds on an existing algorithm named GALFIT[5] (Peng et al. 2002), which is a 2D parametric galaxy fitting algorithm, in the same spirit as other widely used 2D image-fitting algorithms (e.g., GIM2D: Simard 1998; Simard et al. 2002; BUDDA: de Souza et al. 2004). GALFIT is a stand-alone program written in the C language, and can be run on most modern operating systems. To read and produce FITS images, GALFIT calls upon the CFITSIO package (Pence 1999). GALFIT is designed to allow for complex image decomposition tasks: by allowing for an arbitrary number and mix of parametric functions (Sérsic, Moffat, Gaussian, exponential, Nuker, etc.), it can simultaneously fit any number of galaxies and their substructures. It is possible to use GALFIT for both interactive analysis and galaxy surveys where complete automation is required. However, automation requires the use of an external "wrapping" algorithm written by the user that takes care of both the pre-processing (object identification, initial parameter estimation) and post-processing (extracting and tabulating fitting parameters) of the fitting results.

2.1. χ^2_ν and Error Analysis

GALFIT is a nonlinear least-squares fitting algorithm that uses the Levenberg–Marquardt technique to find the optimum solution to a fit. The Levenberg–Marquardt algorithm is currently the most efficient one for searching large parameter spaces, allowing for the possibility of fitting complex images with multiple components and a large number of parameters. GALFIT determines the goodness of fit by calculating χ^2 and computing how to adjust the parameters for the next step. It continues to iterate until the χ^2 no longer decreases appreciably. The indicator of goodness of fit is the *normalized* or reduced χ^2, χ^2_ν:

$$\chi^2_\nu = \frac{1}{N_{\rm dof}} \sum_{x=1}^{nx} \sum_{y=1}^{ny} \frac{(f_{\rm data}(x, y) - f_{\rm model}(x, y))^2}{\sigma(x, y)^2}, \quad (1)$$

where

$$f_{\rm model}(x, y) = \sum_{\nu=1}^{m} f_\nu(x, y; \alpha_1, \ldots, \alpha_n). \quad (2)$$

Here $N_{\rm dof}$ is the number of degrees of freedom in the fit; nx and ny are the x and y image dimensions; and $f_{\rm data}(x, y)$ is the image flux at pixel (x, y). The $f_{\rm model}(x, y)$ is the sum of m functions of $f_\nu(x, y; \alpha_1, \ldots, \alpha_n)$, with n free parameters $(\alpha_1, \ldots, \alpha_n)$ in the 2D model. The uncertainty as a function of pixel position, $\sigma(x, y)$, is the Poisson error at each pixel, which can be provided as an input image. If no σ-image is given, one is generated based on the gain and read-noise parameters contained in the image header. Pixels in the image marked as being bad do not enter into the calculation of χ^2.

In the Levenberg–Marquardt algorithm, the minimization process involves computing a Hessian matrix, which is closely related to the covariance matrix of the parameters (e.g., see Press et al. 1992). The covariance matrix is then directly related to the formal uncertainty in the fitting parameters that GALFIT reports. However, the usefulness of the formal uncertainty is limited to ideal situations where the fluctuations in the residual image are only due to Poisson noise after removing the model. This situation is mostly realized in idealized situations, such as image simulations. In real images, the residuals are due to

[5] http://users.obs.carnegiescience.edu/peng/work/galfit/galfit.html

structures like stars and galaxies that are not fitted, flat-fielding errors, and imperfect functional match to the data. These factors cause formal uncertainties reported in numerical fits to be only lower estimates. In image fitting, more realistic uncertainties are necessarily obtained by other processes, such as comparing fit results based on different assumptions about the model rather than through a formal covariance matrix.

In summary, the three images GALFIT takes as input to calculate least squares are the data, a σ-image, and an optional bad pixel mask. To account for image smearing by the PSF, GALFIT will also require a PSF image.

2.2. Accounting for Telescope Optics and Atmospheric Seeing

The wavefront of light from distant sources is always perturbed by the act of producing an image, distortions due to imperfect optics, and sometimes by Earth's atmosphere, resulting in some blurring. To accurately compare the intrinsic shape of an object with a model, image blurring must be taken into account. In image fitting, this is often done by convolving a model image with the input PSF before comparing with the data. The process of performing convolution is mathematically rigorous, but the actual implementation has several subtleties.

One consideration is the computation speed, as the process of convolving a model is frequently the most time-consuming part of parametric fitting. The trade-off is that the smaller the convolution region, the faster the computation time, but also the less accurate. To achieve a compromise, GALFIT allows the user to decide on the size of the convolution region. This gives the flexibility for one to hone in on a solution quickly before trying to obtain higher accuracy in the final step.

Another important issue to consider is whether to convolve each component separately or all of them together just once in the final image. This is an important consideration because even though the model functions are analytic, they are resampled by discrete pixel grids, resulting in a "pixellated" profile instead of one that is infinitely smooth. If an intrinsic model is sufficiently sharp, the curvature may not be critically subsampled by the pixels prior to convolution, regardless of whether the recorded data are Nyquist sampled. The resulting profile after image convolution therefore can depend very sensitively on how the model is centered on a pixel. If such a model is created off-center, pixellation effectively broadens out the model ever so slightly more than normal once convolution is applied, but the effect is noticeable in high-contrast imaging studies. Therefore, the better way to deal with "pixellation broadening" is to convolve each model component individually rather than the entire image at once. To do so, GALFIT creates every model on a pixel center; the pixel fluxes near the center of the models are integrated over the pixel area adaptively. Then to effect an off-centered model, GALFIT makes use of the convolution theorem by shifting the PSF by the required amount before convolving it with the model. This process circumvents the problem of artificial pixellation broadening because whereas the model core region may not be sufficiently resolved, the PSF ought to be.[6]

Shifting the PSF, however, can be quite problematic when it is marginally Nyquist sampled, or if the diffraction patterns are not critically sampled. Accurate shifting of the PSF is of basic importance in high-contrast imaging studies. For instance, in the case of studying active galaxies with a strong central point source, issues of contrast, resolution, and sampling all conspire to make the PSF fitting crucial to deriving a reliable host model. In such situations, the standard interpolation techniques (e.g., linear or spline) tend to broaden out the PSF core, so they are only accurate in the extended outskirts where the gradient is shallow. One alternative is to interpolate using the sinc kernel, which is theoretically the perfect interpolation kernel for critically sampled images, and preserves the intrinsic width of the data. However, significant "ringing" appears around sharp features (i.e., PSF or galaxy core). This effect can be nearly as bad on a fit as pixellation broadening. An improved solution is to taper the wing of the sinc kernel using a windowing function (e.g., Lanczos), but the ringing often may still be quite large beyond the PSF core, which must be further suppressed.

GALFIT seeks a compromise by using a hybrid scheme where the interpolation in the PSF core is done by using a sinc kernel with a Kaiser window function so as to faithfully preserve the width, but a bicubic spline interpolation is used in the wings. The result of this scheme is that for a Gaussian having an FWHM of 2 pixels, the interpolation is accurate to 0.1% in the center, and 0.03% at the distance of the FWHM relative to the peak (or 1% relative to the local flux). For oversampled PSFs, the interpolation is even more accurate. Compared to bicubic spline interpolation, our scheme is about 20 times more accurate. From a more practical standpoint, the mismatch in the PSFs between data taken using the *Hubble Space Telescope* (*HST*) imaging cameras and synchronously observed PSFs is rarely better than 3% in the core. For all practical purposes, our interpolation scheme therefore will more than suffice for the most demanding high-contrast studies of quasar host galaxies at high redshift.

When the data are undersampled, convolution of the model can still be done correctly if the convolution PSF provided to GALFIT is either critically sampled or oversampled. In this situation, GALFIT will generate a model on a finer grid, convolve it with the PSF, then bin the result down to the resolution of the data for comparison. One way for users to obtain an oversampled PSF compared to the data is to dither the PSF observations by fractional pixels. Another way is to numerically reconstruct a more oversampled PSF star by extracting multiple stars from the data image itself (e.g., via DAOphot, Stetson 1987).

However, lastly, we note that when the data and the convolution PSF are *both* undersampled (i.e., with PSF FWHM < 2 pixels), convolution cannot be done accurately. In such a situation, for the purpose of image fitting, it is often better to broaden out the data and the PSF to critical sampling than to perform the analysis in the original resolution (Kim et al. 2008a).

2.3. The Concept of a Model Component

Using the new features, each model can take on a shape that is completely unrecognizable from a traditional ellipsoid shape. It is therefore necessary to clarify what constitutes a single model component. In GALFIT, *each model component* is referred to by the name of the *surface brightness profile*, just as it is standard practice to call something a Sérsic, Gaussian, or exponential component in traditional models. As implied by this notion, *no matter how complex the shape*, the flux declines monotonically (unless modified by a truncation function, Section 5) from a peak in every radial direction in a non-rotating frame, or along an arc in a rotating frame, strictly following the functional form specified by the user. The radial profile parameters are mathematically decoupled from the azimuthal shape because the radial profile functions are self-similar in the expression of the radius parameter, i.e., with powers of (r/r_e), whereas the complex azimuthal shapes are obtained by simply stretching

[6] If the PSF is not resolved, then the convolution process will not be accurate regardless of the technique.

```
 # IMAGE and GALFIT CONTROL PARAMETERS
 A) gal.fits            # Input data image (FITS file)
 B) imgblock.fits       # Output data image block
 C) none                # Sigma image name (made from data if blank or "none")
 D) psf.fits   #        # Input PSF image and (optional) diffusion kernel
 E) 1                   # PSF fine sampling factor relative to data
 F) none                # Bad pixel mask (FITS image or ASCII coord list)
 G) none                # File with parameter constraints (ASCII file)
 H) 1    200  1    100  # Image region to fit (xmin xmax ymin ymax)
 I) 100    100          # Size of the convolution box (x y)
 J) 20.000              # Magnitude photometric zeropoint
 K) 1.000  1.000        # Plate scale (dx dy)   [arcsec per pixel]
 O) both                # Display type (regular, curses, both)
 P) 0                   # Choose: 0=optimize, 1=model, 2=imgblock, 3=subcomps

# INITIAL FITTING PARAMETERS
#
#   For component type, the allowed functions are:
#       sersic, expdisk, edgedisk, devauc, king, nuker, psf,
#       gaussian, moffat, ferrer, and sky.
#
#   Hidden parameters will only appear when they're specified:
#       Bn (n=integer, Bending Modes).
#       C0 (diskiness/boxiness),
#       Fn (n=integer, Azimuthal Fourier Modes).
#       R0-R10 (coordinate rotation, for creating spiral structures).
#       To, Ti, T0-T10 (truncation function).
#
# ------------------------------------------------------------------------------
#   par)    par value(s)    fit toggle(s)    # parameter description
# ------------------------------------------------------------------------------

# Component number: 1
 0) sersic3 /              #  Component type
 1) 50.0000  50.0000  1 1  #  Position x, y
 3) 15.0000     1          #  Surface brghtnss @ outer R_break [mag/arcsec^2]
 4) 30.0000     1          #  R_e (effective radius)   [pix]
 5) 4.0000      1          #  Sersic index n (de Vaucouleurs n=4)
 9) 0.7000      1          #  Axis ratio (b/a)
10) -30.0000    1          #  Position angle (PA) [deg: Up=0, Left=90]
Ti)  2                     #  Inner truncation by component number(s)
F5) 0.1500   20.0000  1 1  #  Azim. Fourier mode 5, amplitude, & phase angle

# Component number: 2
T0) radial                 #  Truncation type (radial, length, height)
T1) 45.0000  45.0000  1 1  #  Position x, y
T4) 8.0000      1          #  Break radius (99% normal flux)    [pixels]
T5) 5.0000      1          #  Softening length (1% normal flux) [pixels]
T9) 0.7000      1          #  Axis ratio (optional)
T10) 45.0000    1          #  Position angle (optional) [deg: Up=0, Left=90]
F1) 0.6000   20.0000  1 1  #  Azim. Fourier mode 1, amplitude, & phase angle
B2) -5.000e+00  1          #  Bending mode 2 amplitude

# Component number: 3
 0) sersic                 #  Component type
 1) 150.0000 50.0000  1 1  #  Position x, y
 3) 7.0000      1          #  Integrated magnitude
 4) 15.0000     1          #  R_e (effective radius)   [pix]
 5) 2.0000      1          #  Sersic index n (de Vaucouleurs n=4)
 9) 0.5000      1          #  Axis ratio (b/a)
10) 0.0000      1          #  Position angle (PA) [deg: Up=0, Left=90]
R0) power                  #  PA rotation func. (power, log, none)
R1) 0.0000      1          #  Spiral inner radius [pixels]
R2) 15.0000     1          #  Spiral outer radius [pixels]
R3) 180.0000    1          #  Cumul. rotation out to outer radius [degrees]
R4) 0.3000      1          #  Asymptotic spiral powerlaw
R9) 10.0000     1          #  Inclination to L.o.S. [degrees]
R10) 45.0000    1          #  Sky position angle
F1) 0.3000   45.0000  1 1  #  Azim. Fourier mode 1, amplitude, & phase angle
F5) 0.1000   90.0000  1 1  #  Azim. Fourier mode 5, amplitude, & phase angle
```

Figure 1. Example of an input file. The object list is dynamic and can be extended as needed. Each model is modified by a mix of higher order Fourier modes, bending modes, truncation, or spiral structure. These parameters produce the models shown in Figure 2.

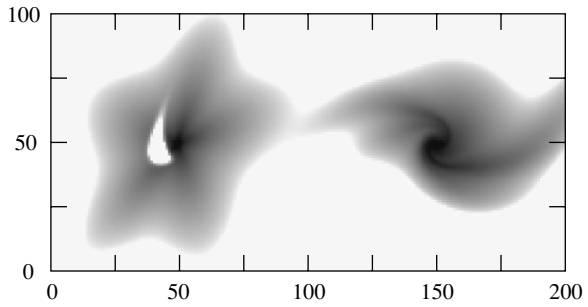

Figure 2. Shapes produced by parameters in the GALFIT input file of Figure 1. Left: a Sérsic light profile modified by a single Fourier mode $m = 5$, creating the star shape. It is truncated in the inner region by a truncation function, which is modified by a bending mode $m = 2$, with a lopsided Fourier mode of $m = 1$. Right: a Sérsic light profile with Fourier modes $m = 1$ and $m = 5$ is modified by a coordinate rotation function to create a lopsided, multi-armed, spiral structure.

the coordinate metric into more exotic grids than the standard Cartesian grid. This idea is in fact implicit in all 2D image-fitting algorithms, where the axis ratio parameter, q, turns a circular profile into an ellipse by compressing the coordinate axis along one direction, even though the functional form of the profile remains the same in every direction. In the same manner, the definition of a scale or effective radius in a component, no matter how complex the shape, corresponds closely to that of the best-fitting ellipse in the direction of the semimajor axis.

Figure 1 demonstrates how Sérsic profiles can be modified by bending modes, Fourier modes, and a spiral rotation function in GALFIT—the results of which are shown in Figure 2. In the example, there are only two Sérsic model components, despite the appearance of numerous parameters: both the "radial" and "power" functions are modifications to the Sérsic profiles. Furthermore, the Fourier and bending modes can modify the Sérsic profiles, or modify the modifiers to the light profiles. Each radial surface brightness profile has a single peak, and the flux decline is monotonic radially (unless truncated by a truncation function called "radial" in Figure 1) or in a rotating coordinate system (called "power" in Figure 1). Therefore, for each component, it is still meaningful to talk about, for example, an *"average" light profile* (e.g., Sérsic), with *an average Sérsic concentration index n*—no matter what the galaxy may look like azimuthally. In this manner, even irregular galaxies can be parameterized in terms of their average light profile. When the average peak of an irregular galaxy is not located at the geometric center, it has a high-amplitude $m = 1$ Fourier mode (i.e., lopsidedness).

In such a way, no matter how complex the azimuthal shape, interpreting the surface brightness profile parameters is just as straightforward as the traditional ellipsoid.

3. THE RADIAL PROFILE FUNCTIONS

The radial profile functions describe the intensity falloff of a model away from the peak, such as the Sérsic, Nuker, or exponential models, among others. For example, early-type galaxies typically have steep radial profiles whereas late-type galaxies have shallower intensity slopes near the center. The rate of decline is governed by a scale-length parameter. The radial profile is often of primary interest in galaxy studies from the standpoint of classification, and because the exact functional form may have some bearing on the path of galaxy evolution. In GALFIT, the radial profile can have the following functional forms, which are some of the most frequently seen in the literature.

The Sérsic profile. The Sérsic power law is one of the most frequently used functions to study galaxy morphology, and has the following form:

$$\Sigma(r) = \Sigma_e \exp\left[-\kappa\left(\left(\frac{r}{r_e}\right)^{1/n} - 1\right)\right], \quad (3)$$

where Σ_e is the pixel surface brightness at the effective radius r_e. The parameter n is often referred to as the concentration parameter. When n is large, it has a steep inner profile and a highly extended outer wing. Inversely, when n is small, it has a shallow inner profile and a steep truncation at large radius. The parameter r_e is known as the effective radius such that half of the total flux is within r_e. To make this definition true, the dependent variable κ is coupled to n; thus, it is not a free parameter. The classic de Vaucouleurs profile that describes a number of galaxy bulges is a special case of the Sérsic profile when $n = 4$ (corresponding to $\kappa = 7.67$). As explained below, both the exponential and Gaussian functions are also special cases of the Sérsic function when $n = 1$ and $n = 0.5$, respectively. As such the Sérsic profile is a common favorite when fitting a single component.

The flux integrated out to $r = \infty$ for a Sérsic profile is

$$F_{\rm tot} = 2\pi r_e^2 \Sigma_e e^{\kappa} n \kappa^{-2n} \Gamma(2n) q / R(C_0; m). \quad (4)$$

The term $R(C_0; m_i)$ is a geometric correction factor when the azimuthal shape deviates from a perfect ellipse. As the concept of azimuthal shapes will be discussed in Section 4, we will only comment here that $R(C_0; m_i)$ is simply the ratio of the *area* between a perfect ellipse with the area of the more general shape, having the same axis ratio q and unit radius. The shape can be modified by Fourier modes (m being the mode number) or diskiness/boxiness. For instance, when the shape is modified by diskiness/boxiness, $R(C_0)$ has an analytic solution given by

$$R(C_0) = \frac{\pi(C_0 + 2)}{4\beta(1/(C_0 + 2), 1 + 1/(C_0 + 2))}, \quad (5)$$

where β is the Beta function. In general, when the Fourier modes are used to modify an ellipsoid shape, there is no analytic solution for $R(m_i)$, and so the area ratio must be integrated numerically.

In GALFIT, the flux parameter that one can use for the Sérsic function is either the integrated magnitude $m_{\rm tot}$ or some kind of surface brightness magnitude, for example, at the center (μ_0), at the effective radius (μ_e), or at the break radius ($\mu_{\rm break}$) for truncated profiles (see Section 5). The integrated magnitude follows the standard definition:

$$m_{\rm tot} = -2.5 \log_{10}\left(\frac{F_{\rm tot}}{t_{\rm exp}}\right) + \text{mag zpt}, \quad (6)$$

where $t_{\rm exp}$ is the exposure time from the image header. Each Sérsic function can thus potentially have seven classical free parameters in the fit: x_0, y_0, $m_{\rm tot}$, r_e, n, q, and $\theta_{\rm P.A.}$. The non-classical parameters, C_0, Fourier modes, bending modes, and coordinate rotation may be added as needed. There is no restriction on the number of Fourier modes, and bending modes, but each Sérsic component can only have a single set of C_0 and coordinate rotation parameters (see Section 4 for details).

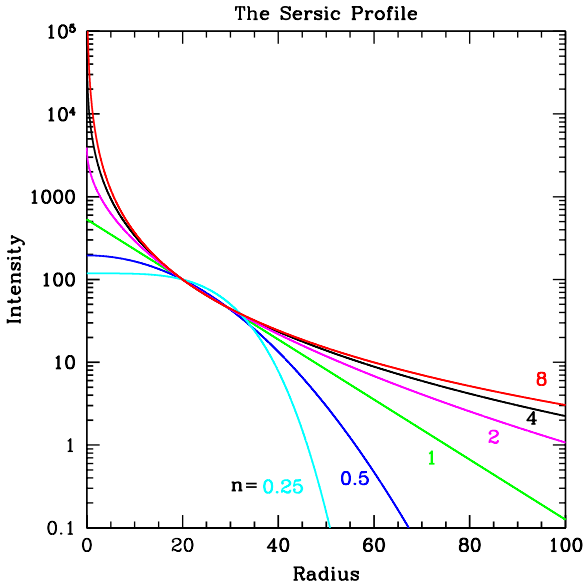

Figure 3. Sérsic profile where r_e and Σ_e are held fixed. Note that the larger the Sérsic index value n, the steeper the central core, and more extended the outer wing. A low n has a flatter core and a more sharply truncated wing. Large Sérsic index components are very sensitive to uncertainties in the sky background level determination because of the extended wings.

(A color version of this figure is available in the online journal.)

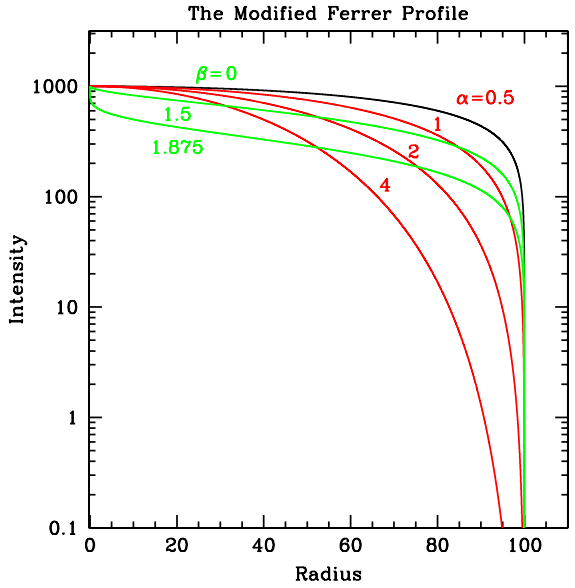

Figure 4. Modified Ferrer profile. The black reference curve has parameters $r_{\rm out} = 100$, $\alpha = 0.5$, $\beta = 2$, and $\Sigma_0 = 1000$. The red curves differ from the reference only in the α parameter, as indicated by the red numbers. Likewise, the green curves differ from the reference only in the β parameter, as indicated by the green numbers.

(A color version of this figure is available in the online journal.)

The exponential disk profile. The exponential profile has some historical significance, so GALFIT is explicit about calling this profile an *exponential disk*, even though an object that has an exponential profile needs not be a classical disk. Historically, an exponential disk has a scale length r_s, which is not to be confused with the effective radius r_e used in the Sérsic profile. For situations where one is not trying to fit a classical disk, it would be less confusing nomenclaturewise to use the Sérsic function with $n = 1$, and quote the effective radius r_e. But because the exponential disk profile is a special case of the Sérsic function for $n = 1$ (see Figure 3), there is a relationship between r_e and r_s, given by

$$r_e = 1.678 r_s \qquad (\text{for } n = 1 \text{ only}). \tag{7}$$

The functional form of the exponential profile is

$$\Sigma(r) = \Sigma_0 \exp\left(-\frac{r}{r_s}\right), \tag{8}$$

and the total flux is given by

$$F_{\rm tot} = 2\pi r_s^2 \Sigma_0 q / R(C_0; m). \tag{9}$$

The six free parameters of the profile are x_0, y_0, $m_{\rm tot}$, r_s, $\theta_{\rm P.A.}$, and q.

The Gaussian profile. The Gaussian profile is another special case of the Sérsic function with $n = 0.5$ (see Figure 3), but here the size parameter is the FWHM instead of r_e. The functional form is

$$\Sigma(r) = \Sigma_0 \exp\left(\frac{-r^2}{2\sigma^2}\right), \tag{10}$$

and the total flux is given by

$$F_{\rm tot} = 2\pi\sigma^2 \Sigma_0 q / R(C_0; m), \tag{11}$$

where FWHM $= 2.355\sigma$. The six free parameters of the profile are x_0, y_0, $m_{\rm tot}$, FWHM, q, and $\theta_{\rm P.A.}$.

The modified Ferrer profile. The Ferrer profile (Figure 4; Binney & Tremaine 1987) has a nearly flat core and an outer truncation. The sharpness of the truncation is governed by the parameter α, whereas the central slope is controlled by the parameter β. Because of the flat core and sharp truncation behavior, historically it is often used to fit galaxy bars and "lenses." The profile,

$$\Sigma(r) = \Sigma_0 \left(1 - (r/r_{\rm out})^{2-\beta}\right)^{\alpha}, \tag{12}$$

is only defined within $r \leqslant r_{\rm out}$, beyond which the function has a value of 0. The eight free parameters of the Ferrer profile are x_0, y_0, central surface brightness, $r_{\rm out}$, α, β, q, and $\theta_{\rm P.A.}$.

It is worth mentioning that a Sérsic profile with low index $n < 0.5$ has similar profile shapes; thus it is often used instead of the Ferrer function.

The empirical (modified) King profile. The empirical King profile (Figure 5) is often used to fit the light profile of globular clusters. It has the following form (Elson 1999):

$$\Sigma(r) = \Sigma_0 \left[1 - \frac{1}{(1 + (r_t/r_c)^2)^{1/\alpha}}\right]^{-\alpha} \times \left[\frac{1}{(1 + (r/r_c)^2)^{1/\alpha}} - \frac{1}{(1 + (r_t/r_c)^2)^{1/\alpha}}\right]^{\alpha}. \tag{13}$$

The standard empirical King profile has a power law with the index $\alpha = 2$. In GALFIT, α can be a free parameter. In this model, the flux parameter to fit is the central surface brightness, μ_0, expressed in mag arcsec^{-2} (see Equation (20)). The other free parameters are the core radius (r_c) and the truncation radius (r_t), in addition to the geometrical parameters. Outside the truncation radius, the function is set to 0. Thus, the total number of classical free parameters is 8: x_0, y_0, μ_0, r_c, r_t, α, q, and $\theta_{\rm P.A.}$.

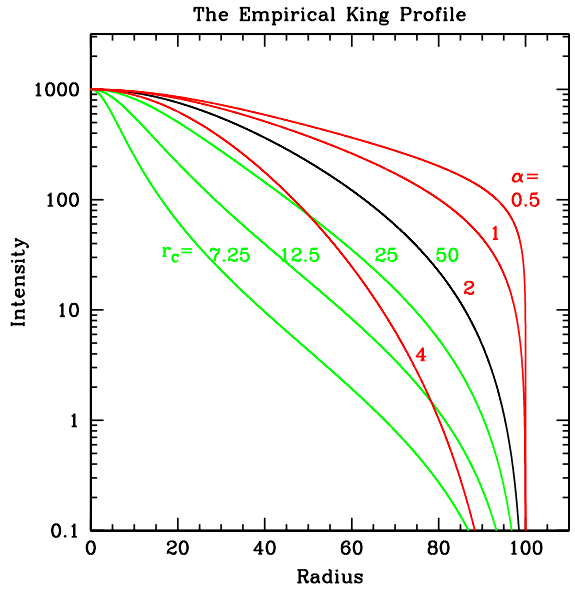

Figure 5. Empirical King profile. The black reference curve has parameters $r_c = 50$, $r_t = 100$, $\alpha = 2$, and $\Sigma_0 = 1000$. The red curves differ from the reference curve only in the α parameter, as indicated by the red numbers. Likewise, the green curves differ from the reference only in the r_c parameter, as indicated by the green numbers.

(A color version of this figure is available in the online journal.)

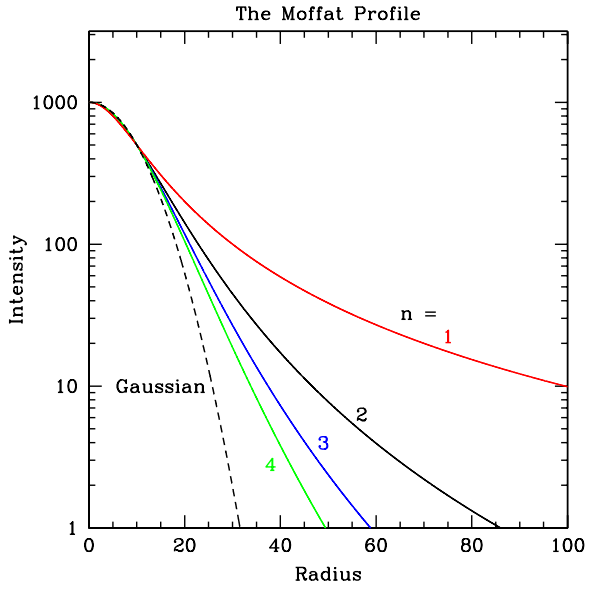

Figure 6. Moffat profile. The black reference curve has parameters $n = 2$, FWHM = 20, and $\Sigma_0 = 1000$. The other colored lines differ only in the concentration index n, as shown by the numbers. The dashed line shows a Gaussian profile of the same FWHM.

(A color version of this figure is available in the online journal.)

The Moffat profile. The profile of the *HST* WFPC2 PSF is well described by the Moffat function (Figure 6). Other than that, the Moffat function (Moffat 1969) is less frequently used than the above functions for galaxy fitting. The functional profile is

$$\Sigma(r) = \frac{\Sigma_0}{\left[1 + (r/r_d)^2\right]^n}, \tag{14}$$

and the total flux is given by

$$F_{\rm tot} = \frac{\Sigma_0 \pi r_d^2 q}{(n-1)R(C_0; m)}. \tag{15}$$

In GALFIT, the size parameter to fit is the FWHM, where the relation between r_d and FWHM is

$$r_d = \frac{\rm FWHM}{2\sqrt{2^{1/n} - 1}}. \tag{16}$$

The seven free parameters are x_0, y_0, $m_{\rm tot}$ (i.e., total magnitude, instead of μ_0) FWHM (instead of r_d), the concentration index n, q, and $\theta_{\rm P.A.}$.

The Nuker profile. The Nuker profile (Figure 7) was introduced by Lauer et al. (1995) to fit the central light distribution of nearby galaxies, and it has the following form:

$$I(r) = I_b\, 2^{\frac{\beta-\gamma}{\alpha}} \left(\frac{r}{r_b}\right)^{-\gamma} \left[1 + \left(\frac{r}{r_b}\right)^{\alpha}\right]^{\frac{\gamma-\beta}{\alpha}}. \tag{17}$$

The flux parameter to fit is μ_b, the surface brightness of the profile at r_b, which is defined as

$$\mu_b = -2.5 \log_{10}\left(\frac{I_b}{t_{\rm exp}\Delta x \Delta y}\right) + \text{mag zpt}, \tag{18}$$

where $t_{\rm exp}$ is the exposure time from the image header, and Δx and Δy are the plate scale in arcsecond. The Nuker profile is a double power law, where (in Equation (17)) β is the outer power-law slope, γ is the inner slope, and α controls the sharpness of the transition. The motivation for using this profile is that the nuclei of many galaxies appear to be fit well in 1D (see Lauer et al. 1995) by a double power law. However, caution should be exercised when using this function because, for example, a low value of α ($\alpha \lesssim 2$) can be mimicked by a combination of high γ and low β (compare Figure 7(c) with the other two panels), which presents a serious potential for degeneracy. In all, there are nine free parameters: x_0, y_0, μ_b, r_b, α, β, γ, q, and $\theta_{\rm P.A.}$.

The edge-on disk profile. Both the Sérsic (Equation (3)) and exponential disk profile (Equation (8)) are merely empirical descriptors of a galaxy light profile. However, for edge-on disk galaxies, there is a more physically motivated light profile: under the assumption that the disk component is locally isothermal and self-gravitating, the light profile distribution is given by van der Kruit & Searle (1981):

$$\Sigma(r, h) = \Sigma_0 \left(\frac{r}{r_s}\right) K_1\left(\frac{r}{r_s}\right) \text{sech}^2\left(\frac{h}{h_s}\right), \tag{19}$$

where Σ_0 is the pixel central surface brightness, r_s is the major-axis disk scale length, h_s is the perpendicular disk scale height, and K_1 is a Bessel function. The flux parameter being fitted in GALFIT is the central surface brightness:

$$\mu_0 = -2.5 \log_{10}\left(\frac{\Sigma_0}{t_{\rm exp}\Delta x \Delta y}\right) + \text{mag zpt}. \tag{20}$$

Note that if the disk is oriented horizontally, the coordinate r is the x-distance (as opposed to the radius) of a pixel from the origin. There are six free parameters in the profile model: x_0, y_0, μ_0, r_s, h_s, and $\theta_{\rm P.A.}$.

The PSF profile. For unresolved sources, one can fit pure stellar PSFs to an image (as opposed to functions with narrow

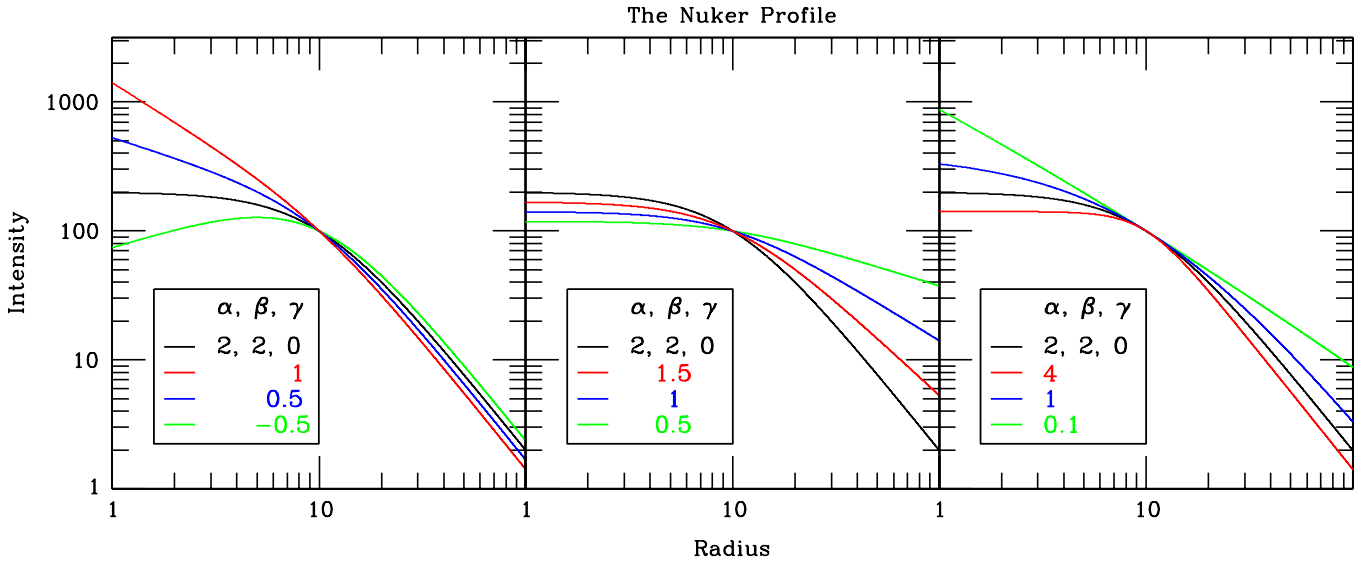

Figure 7. Nuker profile. The black reference curve has parameters $r_b = 10$, $\alpha = 2$, $\beta = 2$, $\gamma = 0$, and $I_b = 100$. For the other colored lines, only one value differs from the reference, as shown in the legend.

(A color version of this figure is available in the online journal.)

FWHM convolved with the PSF). The PSF function is simply the convolution PSF image that the user provides, so there is no prescribed analytical functional form. This is also the only profile that is not convolved in GALFIT. The PSF has only three free parameters: x_0, y_0, and $m_{\rm tot}$. Because there is no analytical form, the total magnitude is determined by integrating over the PSF image and assuming that it contains 100% of the light. If the PSF wing is vignetted, there will be a systematic offset between the flux GALFIT reports and the actual value.

If one wants to fit this "function," it is important to make sure that the input PSF is close to, or super-, Nyquist sampled. The PSF interpolation used in shifting is done by a sinc function with a Kaiser window, which can preserve the widths of the PSF even under subpixel shifting. This is, in principle, better than spline interpolation or other high-order interpolants. However, if the PSF is undersampled, aliasing will occur, and the PSF interpolation will be poor. In this situation, it is better to provide an oversampled PSF to GALFIT (and to specify the amount of oversampling), even if the data are undersampled. With *HST* data this can be done using TinyTim (Krist & Hook 1997) or by combining stars. GALFIT will take care of rebinning during the fitting.

Note that the alternative to fitting a PSF is to fit a Gaussian with a small width (e.g., 0.4–0.5 pixels), which GALFIT will convolve with the PSF. This is generally not advisable if a source is a pure point source because convolving a narrow function with the PSF will broaden out the overall profile, even if slightly. The convergence can also be poor if the FWHM parameter starts becoming smaller than 0.5 pixels. However, this technique can still be useful to see if a source is truly resolved.

The background sky. The background sky is a flat plane with a flux gradient along x- and y-directions. Thus it has a total of three free parameters. The pivot point for the sky is *fixed* to the geometric center (x_c, y_c) of the image, calculated by $(n_{\rm pix}+1)/2$, where $n_{\rm pix}$ is the number of pixels along one dimension. The tip and tilt are calculated relative to that center. Because the galaxy centroid located at (x, y) is in general not at the geometric center (x_c, y_c) of the image, the sky value directly beneath the galaxy centroid is calculated by

$$\mathrm{sky}(x, y) = \mathrm{sky}(x_c, y_c) + (x - x_c)\frac{d\mathrm{sky}}{dx} + (y - y_c)\frac{d\mathrm{sky}}{dy}. \quad (21)$$

4. THE AZIMUTHAL SHAPE FUNCTIONS

Whereas the radial profile governs the decline of galaxy flux radially from a central peak, the azimuthal functions generate the projected shape in the x–y plane of the image. For instance, ellipsoidal, irregular, spiral, disky, and boxy shapes are all created by azimuthal functions. All traditional 2D image-fitting techniques use an ellipse as the fundamental shape, which is obtained by stretching the coordinate grid along one dimension compared to the orthogonal direction. Indeed, all azimuthal functions are coordinate transformations. Therefore, to change a shape from an ellipse into more exotic shapes, the coordinate system $[r(x, y)]$ can be further stretched or shrunk radially from the peak, as a function of azimuth angle. This coordinate transformation preserves the functional form of the surface brightness profile in every direction because the profiles are self-similar—that is, they are functions of $(r/r_{\rm scale})$. Thus defined, the radial profile parameters (e.g., r_e, q, central concentration, etc.) retain their original meaning regardless of the complexity of the azimuthal shape.

We introduce four new ways to modify the azimuthal shape of a model, beginning with the traditional ellipsoidal model. On top of an ellipsoid, this section describes how one can add Fourier modes, bending modes, and coordinate rotation functions (power law and logarithmic). Each component can be modified by any one or all of the azimuthal functions simultaneously, depending on the complexity of the galaxy one is trying to analyze. The following section will cover truncation functions.

Generalized ellipses. The simplest azimuthal shape in GALFIT is the traditional generalized ellipse. This is the starting point for all GALFIT analysis, no matter how complex is the final outcome.

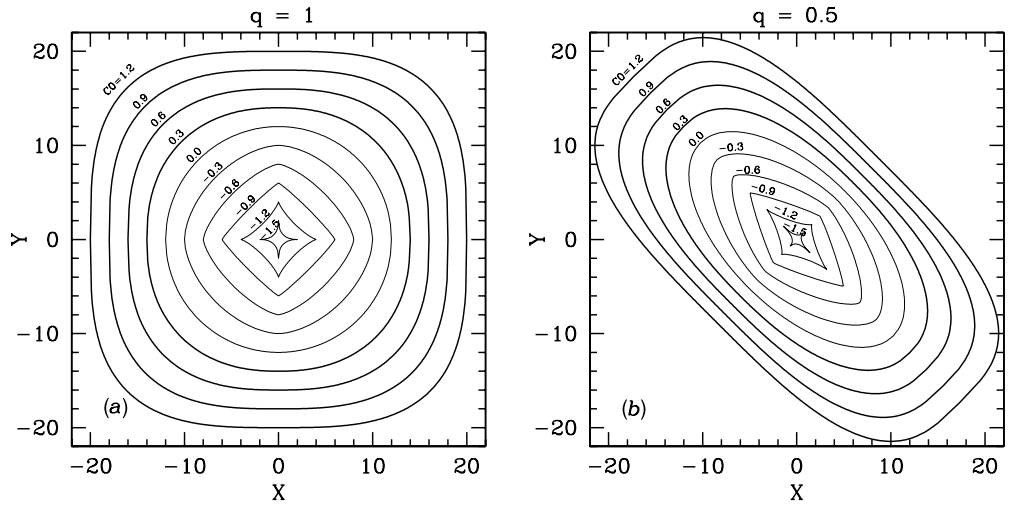

Figure 8. Generalized ellipses with (a) axis ratio $q = 1$ and (b) axis ratio $q = 0.5$. Various values of the diskiness/boxiness parameter C_0 are labeled.

The radial coordinate of the generalized ellipse is defined by

$$r(x, y) = \left(|x - x_0|^{C_0+2} + \left| \frac{y - y_0}{q} \right|^{C_0+2} \right)^{\frac{1}{C_0+2}}. \quad (22)$$

Here, the ellipse axes are aligned with the coordinate axes, and (x_0, y_0) is the centroid of the ellipse. Defined by Athanassoula et al. (1990), the ellipse is called "general" in the sense that C_0 is a free parameter, which controls the diskiness/boxiness of the isophote. When $C_0 = 0$, the isophotes are pure ellipses. With decreasing C_0 ($C_0 < 0$), the shape becomes more disky (diamond-like), and conversely, more boxy (rectangular) as C_0 increases ($C_0 > 0$; see Figure 8). The major axis of the ellipse can be oriented to any P.A. Thus, there are a total of four free parameters $(x_0, y_0, q, \theta_{\rm P.A.})$ in the standard ellipse and an additional one, C_0, for the generalized ellipse.

Fourier modes. Few galaxies look like perfect ellipsoids, and one can better refine the azimuthal shape by adding perturbations in the form of Fourier modes. The Fourier perturbation on a perfect ellipsoid shape is defined in the following way:

$$r(x, y) = r_0(x, y) \left(1 + \sum_{m=1}^{N} a_m \cos\left(m(\theta + \phi_m)\right) \right). \quad (23)$$

In the absence of Fourier modes in the parenthesis, the $r_0(x, y)$ term is the radial coordinate for a traditional ellipse, and $\theta = \arctan\left((y - y_0)/((x - x_0)q)\right)$ defined in Equation (22). The Fourier amplitude for mode m is a_m. Defined as such, a_m is the fractional deviation in radius from a generalized ellipse of Equation (22). The number of modes N is unrestricted, and any mode can be left out. The "phase angle," ϕ_m, is the relative alignment of mode m relative to the P.A. of the generalized ellipse; the phase angle is 0° in the direction of the semimajor axis of the generalized ellipse (rather than up), increasing counterclockwise. Figure 9 shows some examples of how Fourier modes modify a circle and an ellipse into other shapes.

Each Fourier mode has two free parameters, a_m and ϕ_m, and the number of modes the user can add is unrestricted. However, the most useful modes are low-order ones ($m = 1, 3, \ldots, 6$). We note that the $m = 2$ mode is partially degenerate with the classical axis ratio parameter, q, for an ellipse. Therefore, the use of $m = 2$ and q, together, should be largely avoided except in some situations (e.g., peanut-looking bulges).

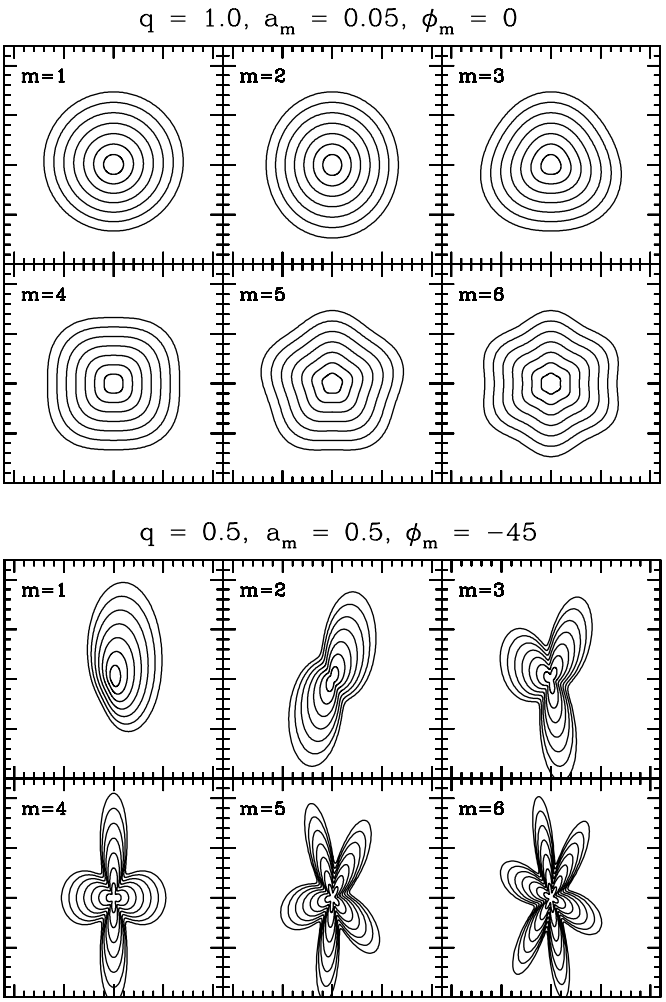

Figure 9. Examples of Fourier modes. Top: low-amplitude ($a_m = 0.05$) Fourier modes modifying a circular profile ($q = 1.0$) with phase angle $\phi = 0°$. Bottom: high-amplitude ($a_m = 0.5$) Fourier modes modifying an elliptical profile ($q = 0.5$) with phase angle $\phi = -45°$.

The phase angles of the Fourier modes are also useful information to keep in mind. Modes with the following phase angles have the following symmetry properties.

1. Symmetry is about a central point: $a_1 = 0$, regardless of other mode phase and amplitude.
2. For all modes m, there is reflection symmetry at $\phi_m = 0^\circ$, $\pm\frac{180^\circ}{m}$. For m = even, this symmetry is about both the major and minor axes, whereas for m = odd, the reflection symmetry is only about the major axis.
3. For odd modes of m, there is additional reflection symmetry about the minor axis at $\phi_m = \pm\frac{90^\circ}{m}$.

An irregular galaxy has angles that are "out of phase" whereas regular galaxies have angles that are more "in phase" (i.e., reflectionally symmetric around either the minor or major axis). Therefore, it is possible to quantify various forms and degree of asymmetry by constructing indices based on the amplitude and phase angles of the Fourier modes. The most intuitively obvious asymmetry index is the $m = 1$ mode, which captures the lopsidedness (A_L) of a galaxy, i.e., the positioning of the brightest central region relative to the fainter outer region of a galaxy:

$$A_L = |a_1| \,. \tag{24}$$

Asymmetric galaxies are also characterized by overall deviation from an ellipse; thus, another intuitively useful quantity to measure is the sum of the Fourier amplitudes:

$$A_E = \sum_m^N |a_m| \,. \tag{25}$$

Asymmetric galaxies by definition have high A_E. However, it is possible for galaxies with both high A_E and A_L to be *reflectionally* symmetric; the degree of reflectional symmetry may be an indicator for how well the galaxies are relaxed. Reflection *asymmetry* is given by the index A_R:

$$A_R = \sum_{m=\text{even}} |a_m| \, \sin^2\left(\pi m \frac{\phi_m}{180^\circ}\right) + \sum_{m=\text{odd}} |a_m| \, \sin^2\left(\pi m \frac{\phi_m}{90^\circ}\right), \tag{26}$$

where ϕ_m is in degrees. In this formulation, the higher the reflectional asymmetry, the higher the index A_R. Used together, these three descriptors provide highly useful ways to quantify the degree galaxies are irregular. For instance, high values of A_R and A_L most likely imply high global asymmetry in the intuitive sense. Whereas a high value of A_E with low A_R implies high regularity, but large deviation from an ellipse, such as edge-on disky galaxies or a disky/boxy ellipticals.

Bending modes. Bending modes allow for power-law-shape curvatures in the model, as opposed to spiral windings. The coordinate transformation $(x, y) \Longrightarrow (x', y')$ is obtained by only perturbing the y-axis (in a rotated frame) in the following way:

$$y' = y + \sum_{m=1}^N a_m \left(\frac{x}{r_{\rm scale}}\right)^m, \tag{27}$$

where $x' = x$, $r_{\rm scale}$ is the scale radius of the model (i.e., $r_{\rm eff}$ for Sérsic, r_s for exponential, etc.). Some examples of this perturbation are shown in Figure 10. Note that $m = 1$ resembles quite closely to the axis ratio parameter, q. However, the $m = 1$ bending mode is actually a shear term, the effect of which is most easily seen when it operates on a purely boxy profile with $C_0 \approx 2$ (Figure 8(a)), shearing it into a more disky shape (see Figure 10(d)). The bending modes can be modified by Fourier modes or diskiness/boxiness to change the higher order shape of the overall model. This kind of coordinate transformation again preserves the original meaning of the radial profiles. Here, the object size parameter refers to the unstretched size, i.e., projected onto the original (x, y) Cartesian frame, as opposed to a length along the curvature.

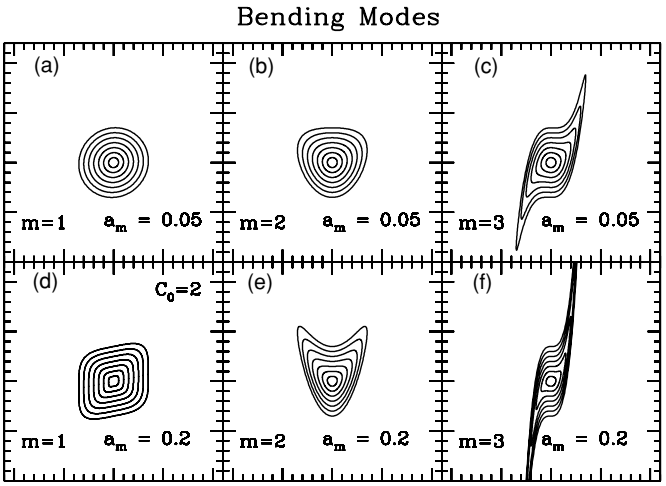

Figure 10. Examples of bending modes modifying a circular profile (q = 1.0) with $C_0 = 0$ (unless indicated otherwise). Top row: low-amplitude ($a_m = 0.05 r_{\rm scale}^m$) bending modes. Bottom row: high-amplitude ($a_m = 0.2 r_{\rm scale}^m$) bending modes. Bending modes can be combined with Fourier modes to change the higher order shape.

Coordinate rotation: the concept. Sometimes the isophotes of a galaxy can rotate as a function of radius, as in the case of spiral galaxies. To model spiral patterns, it is now possible to allow for coordinate rotation in GALFIT. Coordinate rotation in GALFIT means that the flux within circular annuli overlayed on a model rotates as a function of radius, i.e., $\theta = f(r)$. The functional form $f(r)$ can be fairly arbitrary but the most familiar pattern in nature is that of a logarithmic spiral, i.e., $\theta \sim \log(r)$. However, many spiral galaxies deviate from logarithmic winding either in the inner region, for instance, due to the presence of a bar, or in the outer region, as might be due to tidal or non-relaxed features. These structures pose a problem when fitting galaxy images because one cannot simply mask out regions of non-interest when the goal might be to obtain the cleanest separation between a spiral and other embedded components. Therefore, a pure logarithmic spiral, while useful to *trace segments* of a spiral, is often not ideal for *fitting* the whole galaxy, but ought to be modified in some ways. For this reason, we introduce the concept of a hyperbolic tangent (tanh) modification to a logarithmic or a power-law spiral.

A pure tanh function looks like Figure 11(a), showing that $f(r)$ asymptotes to constant values at $r \rightarrow \pm\infty$, which is a highly desirable feature. As shown in Figure 11(a), the function can be scaled, stretched, and shifted so that $\theta(r) \approx 0$ at $r < r_{\rm in}$: it is useful to model a bar-like feature, which, by definition, has a constant P.A. as a function of radius. A tanh function is also useful in the upper asymptotic limit because $f(r)$ at

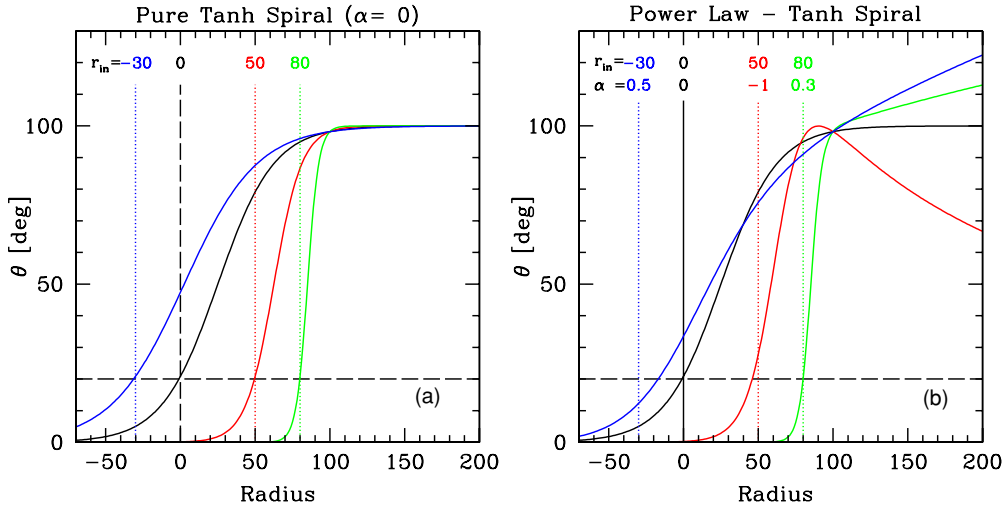

Figure 11. Hyperbolic tangent-power-law spiral angular rotation functions with outer spiral radius of $r_{\rm out} = 100$. (a) Examples of pure hyperbolic tangent spirals ($\alpha = 0$) with different bar radii ($r_{\rm in}$). (b) Examples with different bar radii and asymptotic power law α, as indicated. See Figures 12 and 13 for examples of how these parameters translate into 2D images.

(A color version of this figure is available in the online journal.)

$r > r_{\rm out}$, when multiplied by another function $f_2(r)$, takes on the form of $f_2(r)$, and the cross talk within $r_{\rm in}$ is minimal, as shown in Figure 11(b). In short, a tanh function allows for a *transition* between *two* functions: a constant function at $r < r_{\rm in}$ and another $r > r_{\rm out}$, for example, a power law or a logarithmic function. Moreover, the rate of that transition can be cleanly *managed* and is easy to interpret. For this reason, a hyperbolic tangent is also a function of choice later on in Section 5 when we present the idea of a truncation function. GALFIT allows for two types of coordinate rotation functions, the power-law spiral (α-tanh), and the logarithmic spiral (log-tanh), both of which are motivated empirically. We note that even though the logarithmic spiral is favored more in the literature, we find that the α-tanh spiral is better able to capture the range of spiral behaviors found in nature because of the one extra degree of freedom in α, which can simulate the behavior of the log-tanh spiral over regimes of interest. We therefore tend to prefer use of the α-tanh coordinate rotation by default. We now give an overview of the two types of coordinate rotation:

Coordinate rotation I: power-law-hyperbolic tangent (α-tanh). The term "power law" refers to the fact that the pure tanh function of Figure 11(a) is multiplied by a function of the form $\sim r^{\alpha}$. The exact functional form of the rotation function is lengthy (see Appendix A), but the schematic functional dependence of the power-law spiral on the parameters is given by the following:

$$\theta(r) = \theta_{\rm out}\ \tanh\left(r_{\rm in}, r_{\rm out}, \theta_{\rm incl}, \theta^{\rm sky}_{\rm P.A.}; r\right) \times \left[\frac{1}{2}\left(\frac{r}{r_{\rm out}} + 1\right)\right]^{\alpha}. \quad (28)$$

As defined, the power-law rotation starts to take hold beyond $r = r_{\rm out}$, and below which the tanh transition dominates. Figure 11 shows a pure hyperbolic tangent rotation function for several different values of the parameter $r_{\rm in}$ (left), and a combination of "bar" ($r_{\rm in}$) parameter and the asymptotic power-law slope α (right), where r is the radial coordinate system and $\theta_{\rm out}$ is the rotation angle roughly at $r_{\rm out}$. The inner radius, $r_{\rm in}$, is defined to be the radius where the rotation reaches roughly 20°. This angle corresponds fairly closely to our intuitive notion of bar length based on examining images, but is not a rigorous, physical definition. The angle $\theta_{\rm incl}$ is the line-of-sight inclination of the disk, where $\theta_{\rm incl} = 0°$ is face-on and $\theta_{\rm incl} = 90°$ is perfectly edge-on.

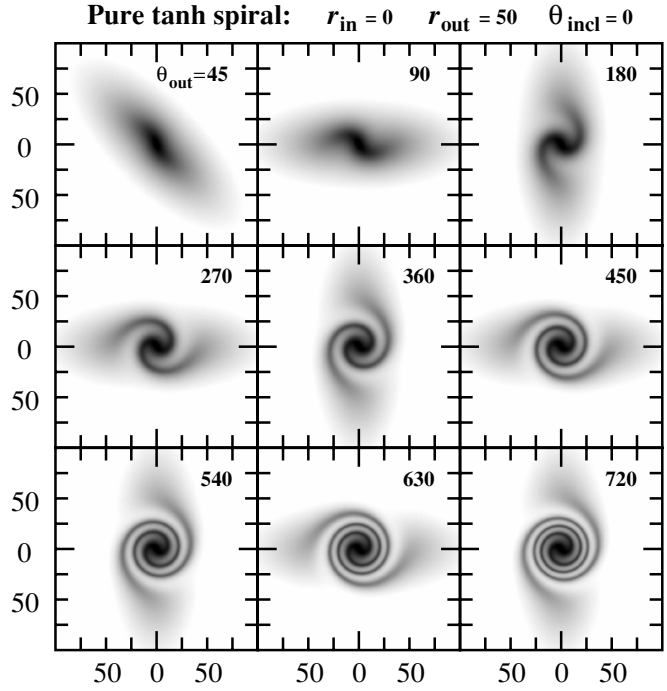

Figure 12. Examples of pure (i.e., with the power law $\alpha = 0$ or without the logarithmic function) hyperbolic tangent coordinate rotation modifying an elliptical profile with axis ratio $q = 0.4$. Note that all the figure panels share the same parameters as shown up top, external to the figures. The spiral model has no bar. The numbers within each panel show the amount of total winding (units are in degrees) at the spiral rotation radius of 50. Note that outside $r = 50$, the rotation angle becomes constant, due to the rotation function being a hyperbolic tangent, thereby creating the appearance of a flattened disk, even though there is not a separate disk component involved in the model.

To motivate intuition for the free parameters used in the coordinate rotation definition, Figures 12 and 13 show a progressive series of images for the spiral rotation function with different combinations of parameter values. For instance, Figure 12 shows a series of images of a pure hyperbolic tanh spiral with increas-

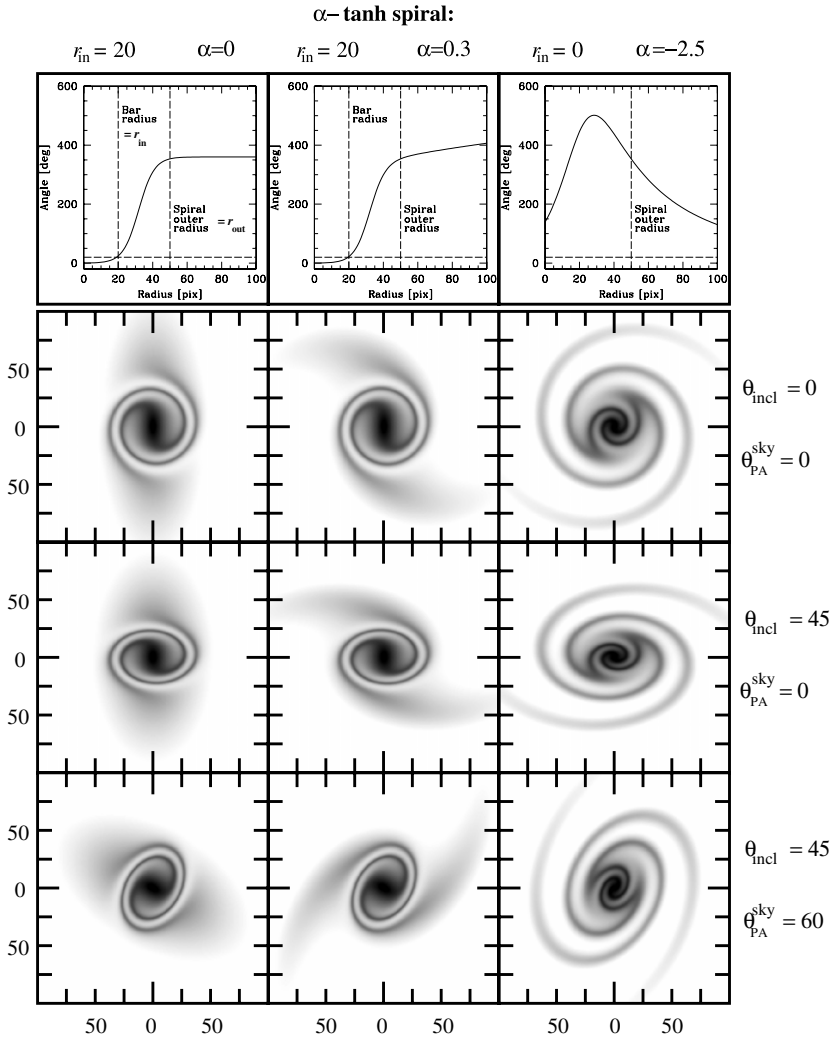

Figure 13. Examples of power-law–hyperbolic tangent (α-tanh) coordinate rotation modifying a face-on ($\theta_{\rm incl} = 0^\circ$) elliptical profile with axis ratio $q = 0.4$. The parameters of the rotation functions are shown on the top and right-hand side of the diagram. The top panels show the spiral rotation angle as a function of radius for the panels in the same column. In the rightmost column, the spiral arms reverse direction at $r = 30$ because the spiral rotation function (top-right panel) decreases with rotation angle.

ing maximum rotation angle ($\theta_{\rm out}$), all else being held constant at the values indicated at the top. The spiral arm winding increases with increasing $\theta_{\rm out}$, and the winding gets tighter, but the body does not expand wider because $r_{\rm out}$ is fixed. It is also important to note that a face-on model does not necessarily mean that the outermost isophotes are round. Rather, the ellipticity of the outermost isophotes is related to the asymptotic behavior of the rotation function, which asymptotes to a constant P.A. beyond a radius of $r_{\rm out}$ for a pure hyperbolic tangent ($\alpha = 0$, Figure 11(a)). The isophotes only appear circular in the main body of the spiral structure when it has a large number of windings. Figure 13 shows several other examples of barred and unbarred spirals, with progressively different α values, sky inclination angle, and rotated to different sky P.A.s ($\theta_{\rm P.A.}^{\rm sky}$). The parameters for each gray-scale figure are shown at the top and to the right of the corresponding column and row. When the power-law index α is negative, the spiral pattern can reverse course after reaching a maximum value (see the rightmost column of Figure 13).

In summary, the hyperbolic tangent power-law function has six free parameters: $\theta_{\rm out}, r_{\rm in}, r_{\rm out}, \alpha, \theta_{\rm incl}$, and $\theta_{\rm P.A.}^{\rm sky}$. The thickness of the spiral structure is controlled by the axis ratio q of the ellipsoid being modified by the hyperbolic tangent, or by the Fourier modes that modify the ellipsoid. To create highly intricate and asymmetric spiral structures, Fourier modes can be used in conjunction with coordinate rotation.

We note that the "bar" radius ($r_{\rm in}$) is a mathematical tool. Even though the $r_{\rm in}$ term in the coordinate rotation does look like a bar when it is sufficiently positive, it should be regarded only as a *mathematical construct* to grant the rotation function as much flexibility as possible. This construct *can* reflect reality, but it does not have to. For instance, mathematically, a *negative* $r_{\rm in}$ radius (Figure 11(b)) is perfectly sensible because of the way Equations (28) and (29) (for logarithmic spirals, below) are defined: a negative $r_{\rm in}$ value just means that the spiral rotation function has a finite rotation angle at $r = 0$ relative to the initial ellipsoid out of which it is constructed. When there is clearly no bar, the $r_{\rm in}$ parameter can become quite negative; in this case, the fit is often indistinguishable from one where the bar radius is 0. Furthermore, often times, one may not wish to create a bar and a spiral out of one smoothly continuous function for various reasons, for instance, because they may have different widths, the spiral may not extend into the center, or the spiral may start off in a ring. In these situations, one can "detach" the bar from the spiral by using a truncation function (see Section 5), by instead

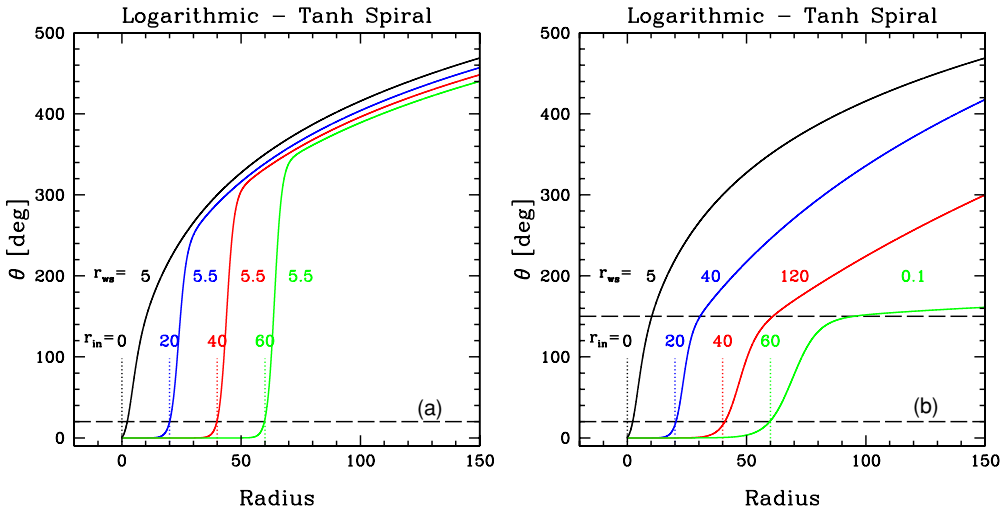

Figure 14. Logarithmic–hyperbolic tangent spiral angular rotation functions. (a) Examples of different bar radii, where the outer hyperbolic spiral radius is $r_{\rm out} = r_{\rm in}+10$. The lower horizontal dashed line shows the rotation angle at the "bar" radius ($r_{\rm in}$). (b) Examples with different "bar" radii ($r_{\rm in}$) and winding-scale radii $r_{\rm ws}$, as indicated, illustrating the degree of flexibility of the spiral rotation rate. The rotation angle at $r_{\rm out}$ is fixed to 150°, as shown by the upper horizontal dashed line. The left-most, black curve is close to being a pure logarithmic function, recasted so that at $r = 0$, the rotation angle $\theta = 0°$.

(A color version of this figure is available in the online journal.)

creating a bar with a separate Sérsic, Ferrer, or other function. When this is done, a "bar radius" is still useful mathematically in the coordinate rotation function, but it may bear no physical relation to the physical bar.

Finally, we draw attention to some limitations of the spiral rotation formulation. While the α-tanh rotation function works surprisingly well for many spiral galaxies, the function is smooth, so "kinks" in the spiral structure cannot yet be modeled, even though it is possible to do so by allowing for "kinks" in the rotation function. Lastly, the spiral structure cannot wind back onto itself, because that would require the rotation function to be multi-valued.

Coordinate rotation II: logarithmic-hyperbolic tangent (log-tanh). The winding rate of spiral arms in late-type galaxies is often thought to be logarithmic with radius rather than power law, with radius. Thus, GALFIT also allows for a logarithmic-hyperbolic tangent coordinate rotation function, which is defined as

$$\theta(r) = \theta_{\rm out}\ \tanh\left(r_{\rm in}, r_{\rm out}, \theta_{\rm incl}, \theta^{\rm sky}_{\rm P.A.}; r\right) \times \left[\log\left(\frac{r}{r_{\rm ws}}+1\right) \Big/ \log\left(\frac{r_{\rm out}}{r_{\rm ws}}+1\right)\right]. \quad (29)$$

Like the α-tanh rotation function, the log-tanh function has a hyperbolic tangent part that regulates the bar length and the speed of rotation within $r_{\rm out}$ (see Figure 15). Beyond $r_{\rm out}$ the asymptotic rotation rate is that of the logarithm function, which has a winding scale radius of $r_{\rm ws}$; the larger the winding scale radius, the *tighter* the winding. Thus, like the α-tanh spiral, the log-tanh spiral rotation function also has six free parameters: $\theta_{\rm out}$, $r_{\rm in}$, $r_{\rm out}$, $r_{\rm ws}$, $\theta_{\rm incl}$, and $\theta^{\rm sky}_{\rm P.A.}$. Note that in terms of capabilities, the α-tanh function can often reproduce the log-tanh function and more. Therefore, the α-tanh is probably a more useful rotation function in practice.

Note that GALFIT does not allow for a pure logarithmic spiral because such a function has a negative-infinity rotation angle at $r = 0$. Therefore, in GALFIT, at $r = 0$ the rotation function reaches $\theta = 0$ (Figure 14). Lastly, it is also important to keep in mind that the meaning of the "bar radius," just as described in the section for α-tanh rotation function, is a mathematical construct.

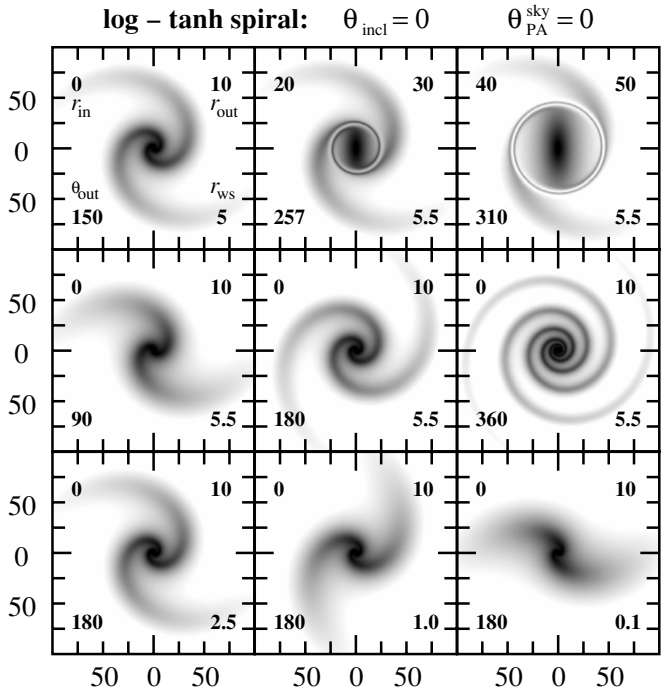

Figure 15. Logarithmic-hyperbolic tangent spiral (log–tanh) angular rotation examples, all face-on ($\theta_{\rm incl} = 0°$) and $\theta^{\rm sky}_{\rm P.A.} = 0°$. The top-left panel shows the meaning of the rotation parameter values at the corners of each box. As with the α-tanh spirals, the log–tanh spiral can be tilted and rotated to any sky projection angle, or combined with Fourier modes to produce lopsided or multi-armed spiral structures (not shown), and with the truncation function to produce an inner ring or an outer taper. The top-left panel figure, for all practical purposes, is a pure logarithmic spiral with a winding scale radius $r_{\rm ws} = 5$.

5. THE TRUNCATION FUNCTION

Truncation functions allow for the possibility of creating rings, outer profile cutoffs, dust lanes, or a composite profile in the sense that the inner region behaves as one function and

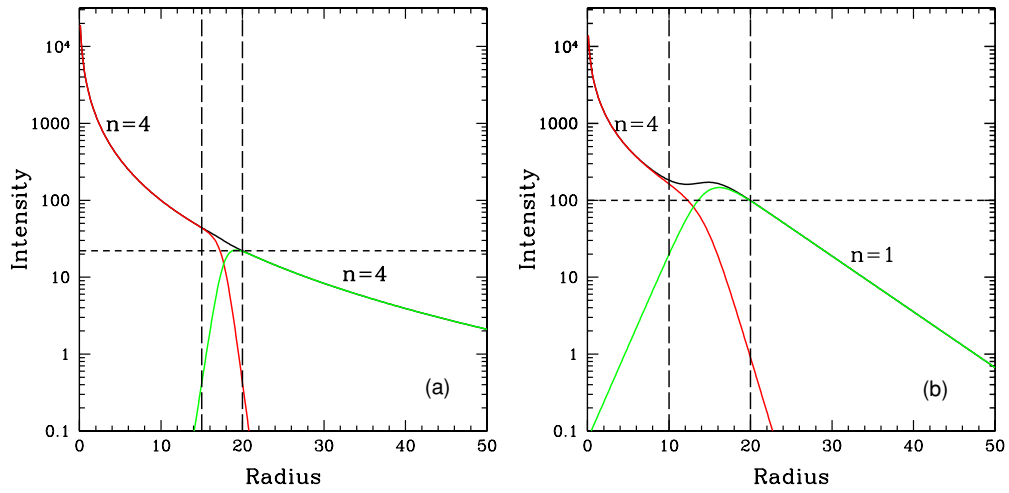

Figure 16. Examples of hyperbolic truncation functions on $n = 4$ and $n = 1$ Sérsic profiles. (a) A continuous $n = 4$ model represented as two truncated models of otherwise identical r_e, n, and central surface brightness, with truncation radii at $r = 15$ and $r = 20$, as marked by the vertical dashed lines. The black curve is the sum of the inner and outer functions. This shows that, outside the truncation region, there is very little "cross talk" between the inner and outer components. (b) A composite profile made up of an $n = 4$ nucleus truncated in the wings and an $n = 1$ truncated in the core, with truncation radii $r = 10$ and $r = 20$. Note that the hump in the summed model would give rise to a ring in a 2D model.

(A color version of this figure is available in the online journal.)

the outer behaves as another. The truncation function can modify both the radial profile and azimuthal shape. A ring can be created by truncating the inner region of a light profile. Likewise, when a galaxy has spiral arms that do not reach the center, it can be viewed as being truncated in the inner region.

5.1. General Principle

In GALFIT, each truncation function can modify one or more light profile models. Also, any number of light profiles can share the *same* truncation function. The truncation function in GALFIT is a hyperbolic tangent function (see Equation (B2) in Appendix B). Schematically, a truncated component is created by multiplying a radial light profile function, $f_{0,i}(x, y; \ldots)$, by one or more truncation functions, P_m or $1 - P_n$ (depending on whether the type is an inner or an outer truncation), in the following way:

$$f_i(x, y; \ldots) = f_{0,i}(x, y; x_{c,i}, y_{c,i}, \ldots, q_i, \theta_{\mathrm{P.A.},i}) \times \prod^{m} P_m(x, y; x_{c,m}, y_{c,m}, r_{\mathrm{break},m}, \Delta r_{\mathrm{soft},m}, q_m, \theta_{\mathrm{P.A.},m}) \times \prod^{n} [1 - P_n(x, y; x_{c,n}, y_{c,n}, r_{\mathrm{break},n}, \Delta r_{\mathrm{soft},n}, q_n, \theta_{\mathrm{P.A.},n})]. \quad (30)$$

The break radius, r_{break}, is defined to be the location where the profile is 99% of the original (i.e., untruncated) model flux at that radius. The parameter Δr_{soft} is the softening length, so that $r = r_{\mathrm{break}} \pm \Delta r_{\mathrm{soft}}$ is where the flux drops to 1% of that of an untruncated model at the same radius (the $\pm$ sign depends on whether the truncation is inner or outer). The inner truncation function (P_m) tapers a light profile in the inner regions of a light profile, whereas the outer truncation function ($1 - P_n$) tapers a light profile in the wings.

The behavior of the hyperbolic tangent function is ideal for truncation because it asymptotes to 1 at the break radius $r \gtrsim r_{\mathrm{break}}$ and 0 at the softening radius $r < r_{\mathrm{soft}}$, and vice versa for the complement function. Thus, when multiplied to a light profile $f(r)$, the functional behavior exterior to the break radius has intuitively obvious meanings. For example, as shown in Figure 16(a), if a Sérsic function with $n = 4$ is truncated in the wings (shown in red), the core has exactly an $n = 4$ profile interior to r_{break} (marked with a vertical dashed line), which is a free parameter to fit. Likewise, an $n = 4$ profile truncated in the core (green) has exactly an $n = 4$ profile exterior to the outer break radius. Thus, when one sums two functions of different Sérsic indices n (Figure 16(b)) the asymptotic profiles of the wing and core retain their original meaning, and there is very little cross talk outside of the truncation region (denoted by vertical dashed lines in Figure 16).

Use of the truncation functions is highly flexible. There can be an unrestricted number of inner and outer truncation functions for each light profile model. Furthermore, multiple light profile models can share in the *same* truncation functions. This is useful, for instance, when trying to fit a dust lane (inner truncation) in a fairly edge-on galaxy that may affect both the bulge and the disk components. Just as with light profile models, the truncation functions can be modified by Fourier modes, bending modes, etc., independent of the higher order modes for the light profile they are modifying.

5.2. Different Variations of the Truncation Function

Truncation models appear in many physical contexts, such as dust lanes, rings, spirals that do not reach the center, joining a spiral with a bar, or cutoff of the outer disk. To allow the truncation parameters to be more intuitive to understand given situations at hand, GALFIT offers several variations. In addition to inner and outer truncations, truncation functions can share in the same parameters as the parent light profile. There are radial and length/height truncations, softening radius versus softening length (default versus type 2), inclined versus non-inclined (default versus type b) truncations, and, lastly, four different ways to normalize the flux—the most sensible choice depends on how a profile is truncated. We now discuss each of these variations in more detail.

Parameter sharing. In the most general form, each truncation function has its own set of free parameters: x_0, y_0, r_{break}, Δr_{soft}, q, and $\theta_{\mathrm{P.A.}}$. However, by default, the parameters x_0, y_0, q, and $\theta_{\mathrm{P.A.}}$ are tied to the light profile model,

and are activated only when the user explicitly specifies a value for them.

Radial ("radial") versus length ("length") or height ("height") truncations. The most useful type of truncation is one that has radial symmetry to first order, i.e., where it has a center, an ellipticity, and an axis ratio. However, in the case of a perfectly edge-on disk galaxy ("edgedisk" model), an additional type is allowed that truncates linearly in length or in height. For instance, a dust lane running through the length of the galaxy has an inner height truncation. For the "edgedisk" profile, GALFIT also allows for a radial truncation, as with all other functions. The one drawback to height and length truncations is that they cannot be modified by Fourier and higher order modes like the radial truncations.

Softening length ("radial") versus softening radius ("radial2"). Sometimes, instead of softening *length* ($\Delta r_{\rm soft}$), it is more useful for the fit parameter to be a softening *radius* ($r_{\rm soft}$), especially when one desires to hold the parameter fixed. That is also allowed in GALFIT as a type 2 truncation function, designated, for example, as "radial2." The default option does not have a numerical suffix.

Inclined (default, "radial") versus non-inclined ("radial-b") truncations.) A spiral rotation function is an infinitesimally thin, planar structure. Nevertheless, it should be thought of as a 3D structure in the sense that the plane of the spiral can be rotated through three Euler angles, not just in P.A. on the sky. When a truncation function is modifying a spiral model, it is therefore sometimes useful to think about the truncation in the plane of the spiral model. When Fourier modes and radial truncations are modifying a spiral structure, the default ("radial") is for the modification to take place in the plane of the spiral structure. However, there are some instances when that may not be ideal (e.g., a face-on spiral may actually be ellipsoidal). In those situations, one can choose "radial-b," which would allow a truncation function to modify the spiral structure in the plane of the sky, even though the spiral structure can tip and tilt as needed.

Lastly, the truncation function can be type 2b (i.e., "radial2-b") as well.

Flux normalization. The most intuitive flux normalization for a truncated profile is the total luminosity. Unfortunately, both the total luminosity and the derivative of the free parameters with respect to the total luminosity are especially time consuming to work out computationally and slow down the iteration process. There are generally no closed form analytic solutions to the problem. Therefore, the alternative is to allow for different ways to normalize a component flux. The user may choose whichever one is more sensible, given the situation and the science task at hand. The default depends on the truncation type.

1. Inner truncation: the flux is normalized at the break radius. This is most sensible for a ring model because this radius roughly corresponds to the peak flux of the ring.
2. Outer truncation: flux normalized at the center.
3. Both inner and outer truncations: same as the case for inner truncation.

However, there are many situations when the default is not desirable. Instead, the user can choose the radius where the flux is normalized. To be pedagogical, we explicitly show here the normalization for just the Sérsic function:

1. *function*: default (e.g., "sersic," "nuker," "king," etc.). See the details for individual functions.
2. *function1*: flux normalized at the center $r = 0$ (i.e., Σ_0). A function that is given originally by $f_{\rm orig}(r)$ is now defined as $f_{\rm mod}(r) = \Sigma_0 \frac{f_{\rm orig}(r)}{f_{\rm orig}(0)}$. For the Sérsic profile (i.e., called "sersic1"), the profile function is redefined in the following way, written explicitly as

$$f_{\rm mod}(r) = \Sigma_0 \frac{\exp\left[-\kappa\left(\left(\frac{r}{r_e}\right)^{1/n} - 1\right)\right]}{\exp\left[\kappa\right]}. \quad (31)$$

   For the Ferrer and King profiles, this normalization is the same as the default normalization.
3. *function2*: flux parameter is the surface brightness at a model's native size parameter (parameter 4 of the light profile model). For a Sérsic profile, called "sersic2," this means the effective radius r_e. So, $f_{\rm mod}(r) = \Sigma_e \frac{f_{\rm orig}(r)}{f_{\rm orig}(r_e)}$. For example, a Sérsic profile now has the following explicit form:

$$f_{\rm mod}(r) = \Sigma_e \exp\left[-\kappa\left(\left(\frac{r}{r_e}\right)^{1/n} - 1\right)\right]. \quad (32)$$

   For the Nuker profile this normalization is the same as the default normalization.
4. *function3*: flux parameter is the surface brightness ($\Sigma_{\rm break}$) at the break radius ($r_{\rm break}$). This is the most useful situation when a truncation results in a large-scale galaxy ring, so that the surface brightness parameter corresponds closely to the peak of the light profile model. When the truncation is not concentric with the light profile model, this kind of normalization is not very intuitive. For "radial" truncation, $r_{\rm break}$ is parameter 4, whereas for "radial2," $r_{\rm break}$ is parameter 4 for outer truncation and parameter 5 for inner truncation. When the "sersic3" option is chosen, the $r_{\rm break}$ parameter comes automatically from the *first* truncation component with which a certain light profile model is associated.
   In our example of the Sérsic profile, $f_{\rm mod}(r) = \Sigma_{\rm break} \frac{f_{\rm orig}(r)}{f_{\rm orig}(r_{\rm break})}$. For example, a Sérsic profile now has the following explicit form:

$$f_{\rm mod}(r) = \Sigma_{\rm break} \frac{\exp\left[-\kappa\left(\left(\frac{r}{r_e}\right)^{1/n} - 1\right)\right]}{\exp\left[-\kappa\left(\left(\frac{r_{\rm break}}{r_e}\right)^{1/n} - 1\right)\right]}. \quad (33)$$

Figure 17 demonstrates just some of the possibilities allowed when fitting truncations. In addition to the regular ellipsoid shape, the higher order modes like diskiness/boxiness parameters, bending modes, and Fourier modes can also modify the shape of the truncation functions. One can also use the truncation function *on* a spiral model, on models with Fourier and bending modes, and diskiness/boxiness models, some of which are shown in Figures 17(d), 17(e), 16(f), and 17(i). When a truncation function acts on a spiral component, it can do so either in the plane of the disk ("type a") or in the plane of the sky ("type b;" e.g., "radial-b"). While the default is in the plane of the disk, the parameters are more intuitive in type b cases when the disk is tilted and rotated.

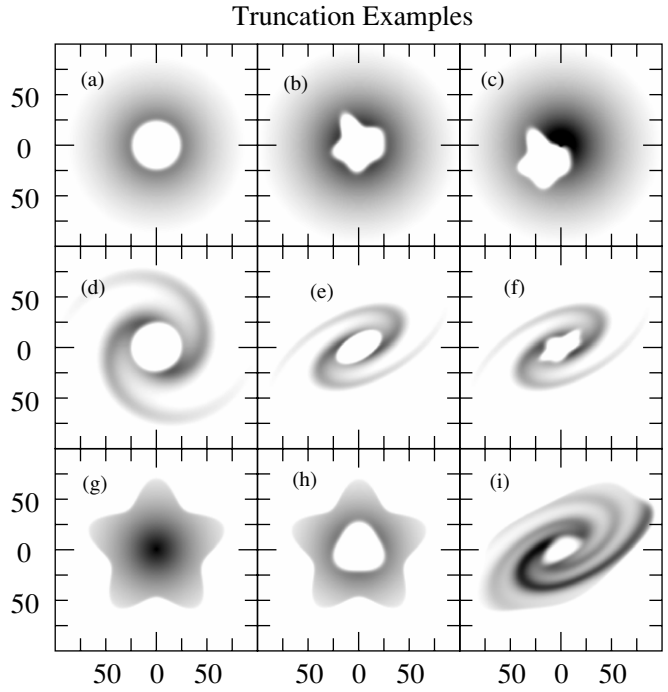

Figure 17. Examples of truncation functions acting on a single-component light profile of various shapes. (a) Inner truncation of a round profile, creating a ring. (b) The truncation function can be modified by Fourier modes, just like the light profile. (c) The truncation function can be offset in position relative to the light profile. (d) The truncation function can act on a spiral model. (e) The truncation can tilt in the same way as the spiral. (f) The truncation function can be modified by Fourier modes while acting on a spiral model. (g) A round light profile is being truncated in the wing by a pentagonal (Fourier mode 5) truncation function. (h) A round light profile is being truncated in the inner region by a triangular function (Fourier mode 3), and in the wing by a pentagonal function. (i) A three-arm, lopsided, spiral light profile model is truncated in the wing by a pentagonal function, and in the inner region by a triangular function.

5.3. Caveats About Using the Truncation Function

The use of truncation functions should be carefully supervised because unexpected things can happen, such as the size or the concentration index of a component can grow without bound. This behavior is due to the fact that there are degeneracies between the sharpness of truncation and the steepness/size of the galaxy. Therefore, truncation functions should only be used on objects that clearly have truncations.

When two functions are joined by using a truncation function, the cross-talk region is located in between the two truncation radii: it is worth bearing in mind the definition that at the break and softening radii, the fluxes are 99% and 1% that of the same model without truncation, respectively. In other words, the larger the truncation length, the larger the cross-talk region. Therefore, when one (or more) of the parameters $r_{\rm break}$, $r_{\rm break}+\Delta r_{\rm soft}$, or $r_{\rm soft}$ is either too small ($\lesssim$ few pixels) or larger than the image size, it probably indicates that profile truncation parameters are not meaningful. Rather, it more likely reveals the fact that there is a mismatch between the light profile model and the actual galaxy profile.

6. INTERPRETATION, PARAMETER DEGENERACIES, UNIQUENESS, LOCAL MINIMA, AND ERROR ANALYSIS

Now that we have introduced several ways to modify an ellipse into more exotic shapes, a natural question to ask is how unique or robust are the modifications. A single-component ellipsoid fit can often be used to quantify the global average profile of galaxies. However, beyond that, decisions about what procedure to use get to be more complicated. On the one hand, the science goal might call for fitting detailed structures inside a galaxy (e.g., a bulge, bar, nuclear star cluster, etc.). On the other hand, doing so raises concerns about parameter degeneracies, uniqueness, and local minima solutions when the analysis becomes complex. It is therefore useful to consider in some depth what causes degeneracies and the different contexts in which they appear. Doing so allows for better understanding for how to deal with them and how to properly interpret results from complex analysis. For, not all complex analyses are more suspect, nor are all simple analyses more robust.

The term "degeneracy" has a specific mathematical connotation, namely, the relation of $a + b = c$ is degenerate in a and b for a constant value of c. In the galaxy fitting literature, "degeneracy" is often more loosely used to also refer to "non-unique" or "local minimum" solutions (e.g., a fit oriented at 90° from the best orientation), or strong "parameter correlation" (e.g., sky is anti-correlated with the Sérsic index n). We will mostly not make the subtle distinctions here and instead will use the term "parameter degeneracy" generically to refer to all such situations.

However, when fitting galaxies, it is more important to distinguish between the aforementioned real degeneracies from "pseudo"-ones. Real degeneracies refer to correlated parameters, local minima, and mathematically degenerate solutions. By contrast, "pseudo"-degeneracies involve convergence issues when an algorithm is used beyond its technical limits, or when users provide bad input model priors to fit the data. They may have nothing to do with real degeneracies, yet the behavior of convergence may seem to suggest otherwise. Whereas problems with real degeneracies are often resolvable by using full spatial information of 2D images, pseudo-degeneracy problems are solved through experience and by using sound scientific or technical judgment, as we elaborate further.

In this section, we discuss how most of the parameter degeneracy problems are avoidable with proper input priors and proper fitting supervision, even when large numbers of free parameters are involved. We also discuss why, contrary to popular notions, when it comes to avoiding model degeneracy and local minima, it is not sufficient to only choose a model that is the simplest. Rather, it is a judicious combination of *simplicity* and *realism* that make for the most robust solutions. Lastly, these discussions are intimately connected to the issue of error analysis because error measurements are nearly always dominated by systematic issues rather than photon noise in galaxy fitting. We therefore discuss why it is more important to quantify model-dependent systematic errors rather than to rely on statistical estimates.

We note that the discussions below are mostly based on experience, which we present using practical examples rather than to show using rigorous proof. Carrying out a rigorous proof is not only beyond the scope of this study, but it is nearly impossible to do in a general manner because different scientific applications have different sensitivities to different types of degeneracies. We are also aware that presenting a full discussion of degeneracy issues lends credence to the common notion that multi-component analysis is dangerously complex. However, the reality is not nearly so dire when one has a proper understanding of the underlying issues and causes.

6.1. True Numerical Degeneracies Caused by Correlated or Non-unique Parameters

There are well-known situations when different parameters in one or more functions are capable of modeling the same profile behavior. This scenario is the one most commonly referred to in generic discussions about model degeneracies. For instance, very large Sérsic index values ($n \gtrsim 4$) have highly extended wings, the presence of which is non-unique with the sky parameter. A high n, caused by profile mismatch or poor model prior, can often suppress the sky estimate. It is therefore advisable to estimate the sky independent of the fit, and to hold it fixed to the best estimate. As a second example, in the Nuker profile (Equation (17)), there are three parameters (α, β, and γ) that control the inner/outer slopes and sharpness of the bending (Figure 7). When the break radius r_b of a Nuker profile is sufficiently small and profile mismatch sufficiently large, model discrimination relies entirely on the power law $\frac{\gamma-\beta}{\alpha}$. Because there are numerous ways to yield a specific value for $\frac{\gamma-\beta}{\alpha}$ in the model, it leads to a degenerate situation involving three parameters.

As another example, a low-amplitude second Fourier mode and the first bending mode (shear) can both be degenerate with the axis ratio q parameter of an ellipse; therefore, they should not be used together except in obvious situations where doing so is useful. Lastly, in the spiral rotation function, the periodicity of the rotation function can sometimes be a source of "degeneracy." Multiple windings can approximate a smooth continuous model, whether or not there is a spiral structure present. For instance, a classical Sérsic ellipsoid can be simulated by a spiral model with a very large $\theta_{\rm out}$. While the fit is not good and easy to diagnose by an end user, it is nevertheless a numerically allowed solution.

The above situations are not meant to be a complete laundry list, but they are the most common situations. In complex analysis, one always needs to be circumspect about the potential hazards of mixing and matching different functions whose parameters produce similar profile behaviors. Even though GALFIT allows for a great deal of flexibility in the analysis, it is ultimately up to the user to decide on what to allow, based on the goals of the science, and to understand when potentially degenerate parameters may be used effectively.

The above discussion may also seem to imply degeneracies or non-uniqueness are too numerous for complex analysis to be practical or reliable. That notion is only true when it is not possible to verify the results of a fit and to try out other solutions. Such a scenario is more common for large-scale galaxy surveys, in which automated, detailed, analysis is admittedly quite difficult to conduct sensibly. However, even in those scenarios, there are many situations where mutually coupled parameters do not affect the other main parameters of scientific interest: degeneracies in the Fourier modes often do not have any bearing on the total luminosity or size of a component. Moreover, when an analysis is done manually, it is reassuring that the problems are almost always easy to recognize and remedy when they do happen, even by simple inspection of the model and residual images.

6.2. Pseudo-degeneracies Caused by Technical Conditions (e.g., Model Profile Resolution, Parameter Boundaries)

Occasionally, what appears to be numerical degeneracy problems may be caused by someone using a code outside the algorithm's physical capabilities. As such, it is a pseudo-degeneracy. Different algorithms have different limitations that affect convergence, whether the code is gradient descent, Metropolis, or otherwise. This situation may appear like parameter degeneracy because restarting the fit does indeed yield a different solution, but in fact the code may be hamstrung in its convergence. For example, gradient descent algorithms require the calculation of a gradient, and thus can run into problems when the gradient cannot be calculated properly. In simulated annealing algorithms (e.g., Press et al. 1992), parameter boundaries and annealing speed control the algorithmic behavior: anneal too quickly, the solution may settle into a local minimum. To search larger parameter spaces requires longer annealing times.

While all algorithms have conditions under which they perform poorly, pseudo-degeneracies can always be recognized and mitigated. GALFIT is based on a Levenberg–Marquardt subroutine that performs the least-squares minimization. In part a gradient descent algorithm, the convergence behavior is affected by the calculation of gradient images that determines the direction of steepest χ^2 descent. When the gradient images are problematic, they affect the convergence to a proper solution. There are three main problematic situations. The first, and most common, occurs when a model becomes extremely compact (FWHM $\lesssim$ 0.5 pixels), so that the profile gradient cannot be resolved: all the gradient information in the model fits into a single pixel. This situation mostly arises when working with high-contrast imaging data, such as quasar host galaxy decomposition, when one of the subcomponents may be used to reduce the strong residuals caused by a PSF mismatch. A similar situation arises when a model is very thin (axis ratio $q \lesssim 0.05$) and the object is compact; here, the gradient does not exist along one spatial direction because of the lack of pixel resolution. Another rare example occurs when the inclination angle of a spiral rotation component is close to perfectly face-on ($\theta_{\rm incl} \rightarrow 0$ in Equations (28) and (29)), when the derivative image for the inclination parameter approaches zero.

Another abnormal numerical behavior may occur when one places parameter constraints on a model to prevent some parameters from wandering too far from their initial values. Doing so may cause poor convergence by forcing the solution into a tight "corner," when the best solution is somewhere beyond it. A typical situation is where there are other sources in the image that are not masked or fitted by models, but that are sufficiently luminous to influence the fit of the target of interest. In this situation, no amount of effort will produce a sensible solution, because the best solution is outside of the parameter boundaries, even though the desired solution may be within. Pseudo-degeneracies occur in this situation both because there is an abnormal condition imposed and because the input prior for the model is poor.

While technical issues with code operation add a layer of complexity to image analysis, in practice the majority of situations one encounters are straightforward to recognize by observing when the parameters take on extremely large or small values. However, clearly recognizing the problem as being pseudo-degeneracies is the key. Once diagnosed, these situations are easy to guard against, by holding those parameters fixed when they go below certain values. In practice, technical issues are not problematic even when GALFIT is used for automated analysis (Häussler et al. 2007).[7]

[7] While these conditions can always be anticipated in advance, implementing a solution in the code is more tricky, because the act of doing so may also induce other convergence difficulties. This leads to a false sense of security about the robustness of a solution.

6.3. Pseudo-degeneracies Caused by Bad Input Model Priors

One of the most common causes of degeneracy problems in galaxy fitting analysis comes from using input priors that are not well suited to the data. The most common "input priors" involve the choice of the type or the number of components in a model.[8] Input priors are ideal when the number of components of a model used in a fit matches the number of luminous components in a galaxy. However, often times one may choose to use either fewer or more components than needed by the data.

A common example where the input prior is bad is when one uses fewer model components than called for by the data. Two of the main reasons for doing so are to reduce the number of components/free parameters, or to allow automated analysis, where it is not yet possible to tailor fits to individual galaxies. This approach is often an intentional course of action taken by many studies, especially when it comes to automating two-component analysis; the goal, ostensibly, is to decompose a galaxy into bulge and disk components. Seemingly reasonable and justifiable on the notion of reducing the potential for degeneracy, the approach is generally regarded by most people to be a positive attribute, rather than a source of problem itself. Yet, that intuitive notion conflicts with the basic principle of how least-squares algorithms work, and leads to perhaps the most common causes of (pseudo-)degeneracy problems cautioned by the literature.

To understand why using fewer components than necessary is bad, it is important to appreciate that galaxy fitting analysis is fundamentally flux weighted. Thus, when a luminous structure is not accounted for, other subcomponents try to compensate, however imperfectly, for its presence. For instance, one may use a two-component model fit to a galaxy that has a bulge, disk, and bar. Doing so may have several different outcomes. One solution is where one component is a sum of (disk+bar) while the other is the bulge. Another can be (bulge+bar) and disk, or perhaps a compromise (e.g., bulge + 0.7 bar; disk + 0.3 bar). Which scenario occurs depends on the relative contrast (i.e., flux weighting) of the bar to the bulge and disk, and potentially on the initial parameters of the three components; small perturbations may "bump" the solution out from one minimum into another. It is quite possible for there to be a "global minimum" solution to this problem. However, when the most meaningful solution, physically, is simply disallowed by the input prior, a globally minimum χ^2 cannot lend much credence to the reality of the model components.

An input model prior might also be bad if the model involves using *more* subcomponents than inherently present in a galaxy. In this situation, the results depend strongly on the degree of profile mismatch between the model function and the data. If there is a significant mismatch, all the components cooperate to reduce the residuals. For instance, it is always possible to fit multiple exponential models to a single-component de Vaucouleurs profile. If the goal is to obtain the total flux, the sum would do a better job than using a single exponential. However, individually, the structural parameters may not have much physical meaning.

Another example involving model prior is in the area of high-contrast imaging, where the goal is to deblend a central, unresolved, point source from a diffuse underlying object (e.g., quasar and host galaxy). To do so reliably requires an accurate PSF model for the unresolved source, or else the residuals may overwhelm the extended object, causing unreliable fits. Here, the prior is the PSF model. Quantifying how the prior affects the fitting results involves trying out different PSFs, or to include extra components to account for the PSF residuals, depending on the science goal.

These examples illustrate some of the most common situations where the reliability of a fit depends less on the number of free parameters and more on having a proper model to describe the data. Beyond a single-component analysis, the need to make such a decision means that it will be difficult to automate highly detailed decompositions of galaxies. However, while multi-subcomponent fitting is difficult to automate, it is reassuring that making a wise decision, interactively, is often not particularly difficult when a science goal is clearly defined. Moreover, for galaxy surveys, where the goal is to fit single-component profiles to galaxies, multi-*object* decomposition is quite feasible to automate (e.g., M. Barden et al. 2010, in preparation; Häussler et al. 2007).

In summary, pseudo-degeneracy conditions exist because least-squares fitting fundamentally involves flux weighting: when luminous flux distributions are present in an image, the models are attracted toward them to reduce the residuals. Therefore, when all components are not properly modeled, the result may be tricky to interpret not because of potential for model degeneracies, but that the solution may have no physical meaning even if there is a global minimum. The solution is to increase the complexity of the analysis progressively until all luminous components are properly accounted. This process does not imply, however, that it is necessary to account for every component inside a galaxy for the solution to have any meaning, only that components of similar flux ratios ought to be simultaneously accounted in detailed analysis; with a few exceptions (e.g., locally dominant features like nuclear star cluster, nuclear ring), components with low fluxes generally do not significantly disturb the parameters of the much more luminous subcomponents.

6.4. Parameter Degeneracies Can be Broken by Spatial Information in 2D

One of the most common notions regarding fitting degeneracy is that the more free parameters there are, the greater is the potential for degeneracy problems. However, the sheer number of parameters is often not itself an indication of a potential for parameter cross talk. Consider, for instance, that it is equally robust to fit thousands of well-separated stars as it is to fit an isolated one. The same is true for galaxies, even though they are considerably more extended and may overlap: in large-scale image simulations, Häussler et al. (2007) studied automated batch analysis of galaxies using one Sérsic profile per galaxy. They find that simultaneously fitting overlapping or neighboring objects using multiple components (often 3–10 Sérsic models at a time) recovers the input simulated parameters more accurately than fitting a galaxy singly while masking out the neighbors.

Indeed, spatially well-localized sources, like a bar, ring, or off-nuclear star clusters, are virtually free from degeneracies caused by cross-talk with other components. A galaxy bar is well determined because it is more elongated, has a flatter radial profile, and is more sharply defined than the surrounding bulge and disk components, despite being embedded within. Compact objects that are off-centered may also be well determined if the rest of the galaxy can be modeled accurately. Contrary to notions that more model components lead to greater degeneracy, it is important to consider the qualitative aspects of those components: not accounting for strong features

[8] An input prior does not refer to the accuracy of the initial parameter guesses.

explicitly can yield a less reliable and less physically meaningful fit because the solution is a compromise between the different subcomponents.

6.5. Measurement Uncertainties, Parameter Correlation, and Parameter Degeneracies

The issue of parameter degeneracies closely ties into the topic of measurement uncertainties, especially when the result of the analysis may depend on the input model in fitting galaxies. When the model fits the data perfectly (i.e., the residuals are only due to Poisson noise) it is possible to infer parameter uncertainties from the covariance matrix of free parameters, which is produced during least-squares minimization by the Levenberg–Marquardt algorithm. In galaxy fitting, ideal situations are often not realized because the differences between the data and the model profile involve not only random (e.g., Poisson) sources, but also systematics from non-stochastic (e.g., profile function or shape mismatch, neighboring galaxies, etc.), and stochastic factors (overall smoothness, for instance, due to star clusters). The one exception is under low S/N situations, when Poisson noise exceeds model imperfection. In most other situations, non-random factors dominate the residuals, causing uncertainties inferred from covariance matrices to be underestimated. Therefore, it is frequently not very meaningful in galaxy fitting to cite measurement uncertainties for the fitting parameters in the traditional sense.

One way to quantify uncertainties, possible in large galaxy surveys, is to allow the *scatter* of the data points in physical relations (e.g., radius versus luminosity, luminosity versus metallicity, etc.) to articulate the overall uncertainty of the measurements, even if individual errors could not be easily obtained. Such a scatter inherently involves a convolution of several error sources: the intrinsic scatter present in a physical relation, Poisson measurement error, stochastic and non-stochastic systematic errors due to model imperfections. Intrinsic scatter, being a fact of nature, remains present in physical relationships even should the data have infinite S/N, and even if the models are perfect fits to the data. Intrinsic scatter is often a scientifically interesting quantity, but it is difficult to differentiate from scatter caused by systematic and stochastic errors, which do not vanish given infinite S/N.

In the absence of large galaxy surveys, it is then important to quantify stochastic and non-stochastic systematic errors for individual objects. Some example situations include the black hole mass versus galaxy relation studies (Kormendy & Richstone 1995; Gebhardt et al. 2000; Ferrarese & Merritt 2000) and the fundamental plane (Djorgovski & Davis 1987).

In general, it is very difficult to pinpoint all the causes of non-stochastic systematic errors in an analysis, and to quantify their magnitude. However, one common cause is profile model mismatch: to the extent that one does not know the intrinsic model of a galaxy a priori, the uncertainty in measuring the parameters is wedded to one's assumptions about the model. Therefore, the process of quantifying systematic, model-dependent errors involves exploring the degree of parameter coupling, by trying out different models and seeing how the parameters of key scientific interest change. Another source of systematic error is due to comparing results from different algorithms. In this scenario, the most sensible practice is therefore to only compare parameters that are derived using the *same fitting technique* (rather than 1D versus 2D), and using the *same pixel and flux weighting scheme* (instead of Poisson versus non-Poisson) during analysis.

In contrast, stochastic errors arising from general non-smoothness of a galaxy profile are caused by, for example, star-forming patches, dust lanes, etc. Existing on small scales and widely dispersed, non-smoothness cannot be easily identified and modeled in a practical manner using multiple components. Even if it is possible to do so, whether they ought to be fitted explicitly, masked, or not treated at all, falls under the purview of the science goal. Stochastic fluctuations often influence the analysis in a manner analogous to having large correlated noise in the data. If the fluctuations can be quantified, one possible solution is to include them in the fit as a variance term of χ^2 (Equation (1)). To estimate the fluctuations requires first obtaining a smooth underlying model, which is not always easy to do if galaxies have steep and/or irregular profiles.

While it is generally difficult to disentangle stochastic from non-stochastic sources of systematic errors, there also do not seem to be obvious benefits for doing so from a scientific standpoint. For most applications, one should only be interested in the overall magnitude of the systematic errors in a collective sense. One way forward is therefore to understand which parameters are most strongly coupled, then compare the results of different solutions judging by which ones are physically plausible. For instance, one common interest in bulge-to-disk (B/D) decomposition is to quantify the uncertainty of the Sérsic index n. We know that the Sérsic index n takes on a large value when a profile has both a steep core *and* an extended wing (see Figure 3). Therefore, quantifying systematic errors in measuring the Sérsic n might involve masking or fitting nuclear sources/neighboring contamination, trying out different PSFs, or fitting the disk by allowing for different disk Sérsic index values. Properly judging the causes of systematic errors and accounting for them often would lead to more natural fits and more sensible parameter values, without the need to hold certain parameters fixed to preconceived answers.

In exploring the parameter space as described, there is often a concern that parameter degeneracies are too numerous or problematic to understand, which brings the discussion back full circle. As discussed in previous sections, when the cause of parameter degeneracy is properly identified, and when the model priors are well conceived, our experience has been that spatial information in 2D can often effectively break many potential degeneracies between the components. Even when the size, luminosity, and central concentration of the different components correlate, they often interact in fairly superficial ways, and do not dramatically change what the model components represent physically. However, in situations where cross talk is significant and there is no reason to prefer one solution over another (when the input prior is befitting), then differences in the answer speak to the degree of the parameter uncertainty that is of key interest to quantify, rather than to avoid, because ultimately the models are empirically motivated.

In summary, to the extent that the results may depend on model assumptions, parameter exploration is the only viable way to quantify true measurement errors in the fit parameters. Thus, when used properly, parameter coupling/degeneracy, rather than complicating the interpretation, offers a deeper insight into the reliability of the overall analysis. We illustrate the above ideas more explicitly in the following examples.

7. EXAMPLES OF DETAILED DECOMPOSITION

To demonstrate how to use the new features to extract complex structures, we analyze five galaxies that are well resolved: IC 4710, an edge-on disk galaxy, Arp 147, M51, and NGC 289.

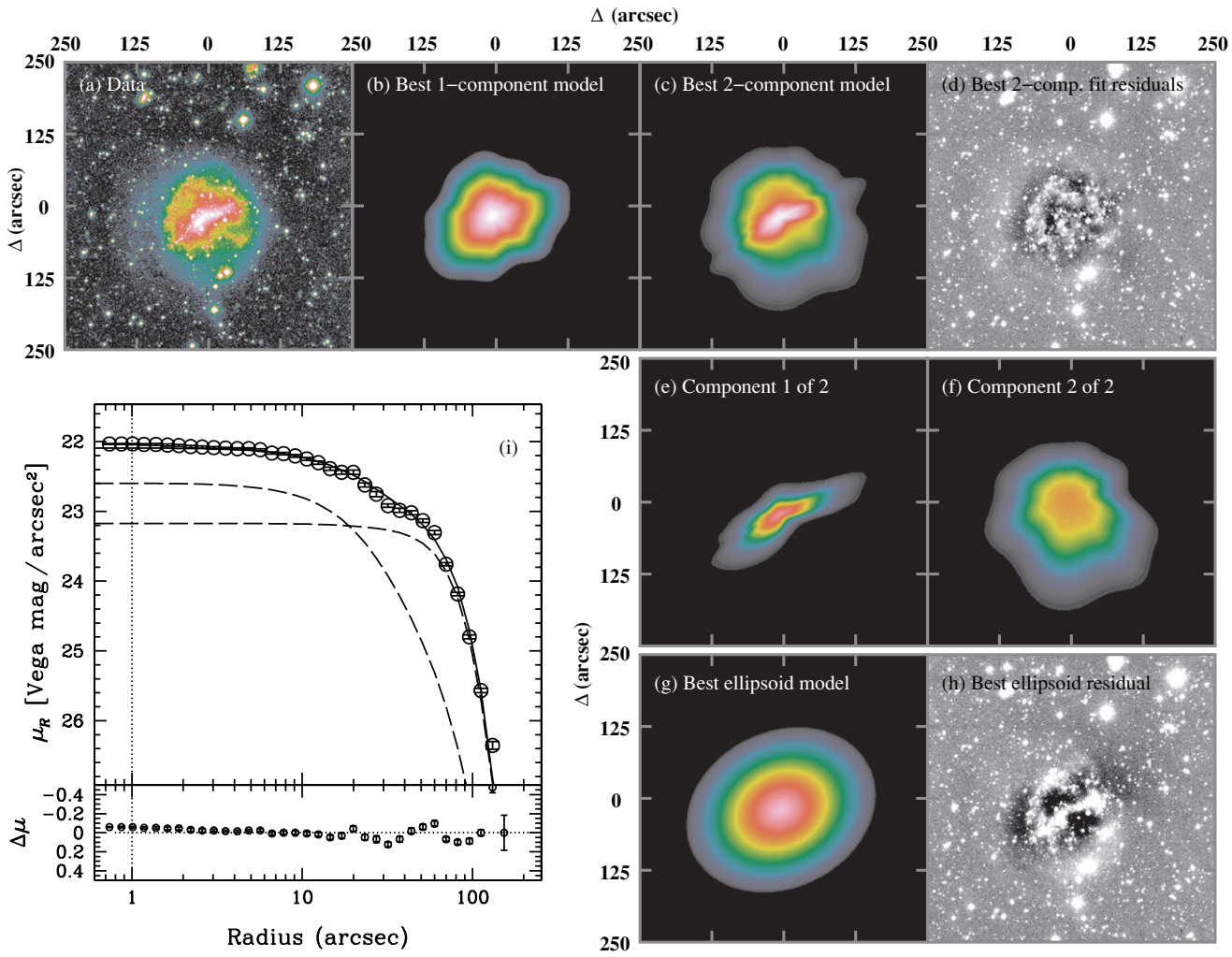

Figure 18. Detailed analysis of IC 4710. (a) Original data. (b) Best single-component Sérsic profile fit with Fourier modes from $m = 1$ to $m = 10$. (c) Best two-component Sérsic profile fit each with Fourier modes, corresponding to the parameters shown in Table 1. (d) Best-fit residuals. (e) Component 1 of 2 in the best-fit model of panel (c). (f) Component 2 of 2 in the best-fit model. (g) A traditional single-component ellipsoid fit. (h) Residuals from the model in panel (g). (i) The 1D surface brightness profile. The individual components are shown as dashed lines, and the solid line coursing through the data is the sum of the two components. The lower panel shows the residuals of data—model.

These galaxies are chosen because they represent examples where traditional analysis using perfectly ellipsoid models tend to leave some question as to what is physically being measured and to the robustness of the photometry and decomposition. The primary purpose here is to illustrate the basic building blocks of galaxy morphology, not to address what are the most "scientifically interesting" or useful applications—the scope of which is far too broad to address. As such, each individual example is not intended to necessarily be "interesting" in its own right. For instance, while parameterizing a ring galaxy like Arp 147 may not itself be too worthwhile scientifically, the concept has other relevance to deblending Einstein rings from lensing galaxies in the image plane of strong gravitational lenses, or separating a ring from a bulge, disk, and bar in spiral galaxies. Indeed, these are heuristic examples meant to generate new ideas for potentially interesting applications, and to illustrate the dynamic range of capabilities in our new approach.

Another goal of this section is to illustrate two seemingly contradictory notions when it comes to galaxy morphology analysis:

1. Sometimes it is not necessary to perform "full-blown" analysis, including spiral structures, Fourier modes, rings, etc. The detailed analysis below will show when it is *not* necessary to utilize the full machinery in order to meet the science requirements, such as when the interest is to only quantify global properties. However, . . .
2. Sometimes it is necessary to perform full-blown analysis. In situations where detailed decomposition matters (e.g., quantifying bulge–disk–bar fractions) the most reliable analysis is to make full use of the machinery available.

Indeed, the availability of new tools does not in any way invalidate or weaken the conclusions of hundreds of studies that came before this one—quite the contrary. Rather, the main message is that given the new capabilities, it is more important now than ever to weigh the relative benefits of sophistication against the drawback of increased difficulty and time, whereas no such options existed before.

7.1. IC 4710

IC 4710 is an SB(s)m galaxy, which has a bar-like feature in the middle of a roundish outer structure, as shown in the *R*-band image of Figure 18, which comes from the Carnegie–Irvine

Table 1
IC 4710 Fitting Results

Parameter	#	– sersic –	Δx ($''$)	Δy ($''$)	mag	r_e ($''$)	n	q	$\theta_{\rm P.A.}$ (deg)	Comments
		fourier	...	mode: ampl. & phase (deg)		mode: ampl. & phase (deg)		mode: ampl. & phase (deg)		
Best fit	1	– sersic –	0.00	0.00	13.71	48.92	0.55	0.32	−63.36	
			0.16	0.08	0.00	0.17	0.00	0.00	0.07	
Inner		fourier	...	1: 0.16	1: −97.40	3: 0.17	3: −17.95	4: 0.06	4: 17.67	
component			...	1: 0.00	1: 1.18	3: 0.00	3: 0.21	4: 0.00	4: 0.32	
		fourier	...	5: 0.05	5: 18.37	6: −0.06	6: 13.22	7: 0.03	7: −1.20	
			...	5: 0.00	5: 0.34	6: 0.00	6: 0.23	7: 0.00	7: 0.63	
		fourier	...	8: 0.05	8: 10.92	9: 0.01	9: 4.55	10: 0.03	10: −6.68	
			...	8: 0.00	8: 0.17	9: 0.00	9: 1.63	10: 0.00	10: 0.29	
Outer	2	– sersic –	1.97	26.28	12.49	57.24	0.37	0.90	41.38	
component			0.24	0.19	0.00	0.09	0.00	0.00	0.85	
		fourier	...	1: −0.31	1: −39.25	3: 0.03	3: 55.46	4: 0.03	4: −27.65	
			...	1: 0.00	1: 0.86	3: 0.00	3: 1.31	4: 0.00	4: 0.89	
		fourier	...	5: 0.04	5: −15.73	6: 0.02	6: −12.47	7: 0.01	7: 16.56	
			...	5: 0.00	5: 0.87	6: 0.00	6: 1.15	7: 0.00	7: 1.74	
		fourier	...	8: −0.03	8: −13.49	9: 0.01	9: −19.63	10: 0.02	10: −15.64	
			...	8: 0.00	8: 0.86	9: 0.00	9: 0.91	10: 0.00	10: 0.92	
		merit	$\chi^2 = 167438.77$		$N_{\rm dof} = 127966$		$N_{\rm free} = 53$	$\chi^2_\nu = 1.31$		
Single	1	– sersic –	0.00	0.00	12.15	60.37	0.69	0.82	−63.51	
component			0.06	0.05	0.00	0.12	0.00	0.00	0.31	
		merit	$\chi^2 = 247304.81$		$N_{\rm dof} = 128009$		$N_{\rm free} = 10$	$\chi^2_\nu = 1.93$		
Single	1	– sersic –	0.00	0.00	12.15	59.00	0.69	0.83	−64.43	
component			0.12	0.09	0.00	0.09	0.00	0.00	0.24	
with		fourier	...	1: −0.05	1: 72.02	3: −0.07	3: 27.55	4: −0.02	4: −7.37	
Fourier			...	1: 0.00	1: 2.39	3: 0.00	3: 0.31	4: 0.00	4: 0.48	
modes		fourier	...	5: 0.02	5: 5.54	6: −0.01	6: −7.72	7: −0.02	7: 15.40	
			...	5: 0.00	5: 0.54	6: 0.00	6: 0.80	7: 0.00	7: 0.33	
		fourier	...	8: 0.01	8: 0.28	9: 0.01	9: 3.16	10: −0.02	10: 1.12	
			...	8: 0.00	8: 0.50	9: 0.00	9: 0.63	10: 0.00	10: 0.25	
		merit	$\chi^2 = 235140.44$		$N_{\rm dof} = 127991$		$N_{\rm free} = 28$	$\chi^2_\nu = 1.84$		

Notes. Best-fitting parameters for IC 4710. The meaning of the object parameters is shown at the top for each model component. The statistical uncertainties for each model component, based on the covariance matrix of the fit, are shown in the row underneath the best-fitting model parameters. Systematic uncertainties due to imperfect model–data match are typically 1%–10% for the fluxes, 10%–20% for the sizes, and 20%–30% for the Sérsic index. For the Fourier modes, the phase angle is relative to the major axis of the light profile component. Note that the sky parameters are not shown. The "*Best fit*" parameters (top section) correspond to panel (c) in Figure 18, "*Single component*" parameters (middle section) correspond to panel (g), and "*Single component with Fourier modes*" parameters (bottom section) correspond to panel (b).

Nearby Galaxy Survey (CINGS) project.[9] Prior to the analysis, we masked out the stars using the SExtractor software (Bertin & Arnouts 1996). We analyze this galaxy using, for comparison, both one- and two-component regular and higher order models with Fourier modes, shown in Figures 18(b)–(i). The best-fit parameters are given in Table 1, which illustrates three different sets of analysis parameters: best fit using two components (Figure 18(c)), a model using just the traditional ellipsoid component (Figure 18(g)), and the same single-component model with Fourier modes added (Figure 18(b)). Figure 18(i) shows the radial surface brightness profile of the data and the individual subcomponents of the best model.

There are several points to understand from comparing detailed and simple analyses. The best-fitting ellipsoid model (Figure 18(g)) is oriented more parallel to the bar-like, higher surface brightness component than the lower surface brightness body; however, the ellipsoid model is much broader than the bar (Figure 18(e)). This happens because a single-component fit is a compromise between the various subcomponents of a galaxy, and, as such, it reflects neither one perfectly. Allowing the azimuthal shape to change by adding nine Fourier modes results in a shape shown in Figure 18(b). Note that because the profile is restricted to having a Sérsic functional form in every direction radially from the peak, the shape does not have complete freedom to take on any shape, as opposed to a shapelet or wavelet-type Fourier inversion: it is merely a higher order perturbation of the best-fitting ellipse. Indeed, in comparing single-component fit parameters in Table 1 for the two models, the main Sérsic structural parameters hardly budged, despite the Fourier model having 18 more free parameters. Therefore, the marginal returns in using more free parameters are negligible in this situation when it comes to the main Sérsic structural parameters. However, if the scientific interest is to quantify the global symmetry, then the higher order modes are of interest.

Another point of interest is how higher order models affect the accuracy of the global photometry. It is natural to expect when a model is unrealistic for a galaxy that the photometry is also unreliable. In Figure 18(c), it is evident that a two-component model is more appropriate than the single-component fits of Figures 18(b) and (g). However, when the flux of the two-component model is summed, one finds that the difference with the single-component fits is only 0.03 mag. This and subsequent examples illustrate empirically that the process of least-squares minimization using even naïve ellipsoids is often capable of

[9] http://users.obs.carnegiescience.edu/lho/projects/CINGS/CINGS.html

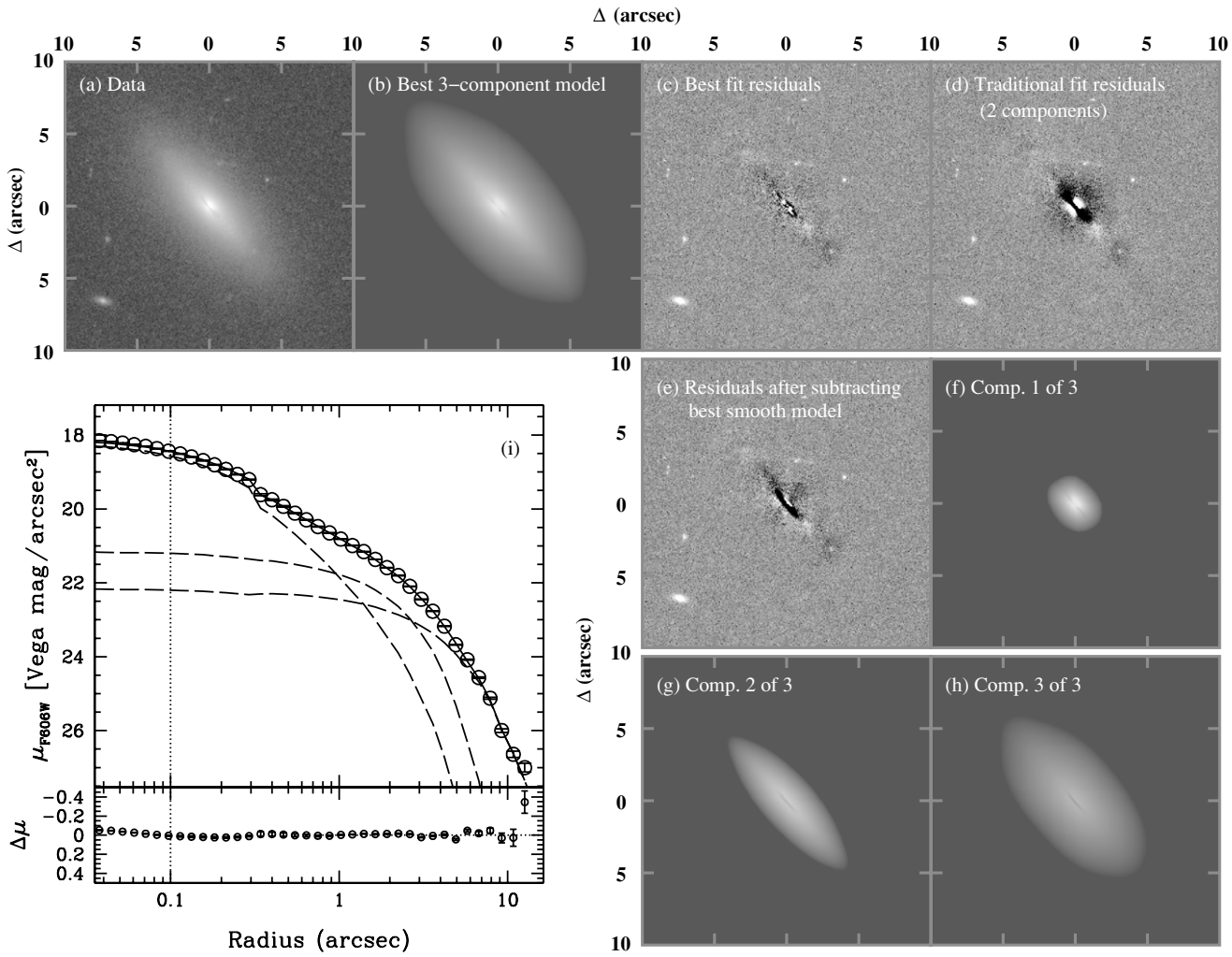

Figure 19. Detailed analysis of an edge-on disk galaxy from GEMS. (a) Original data. (b) Best two-component Sérsic profile fit each with Fourier modes, corresponding to the parameters shown in Table 2. (c) Best-fit residuals. (d) The fit residuals using traditional (i.e., purely ellipsoid) models without masking the dust lane. (e) Residuals after subtracting the best traditional models, masking out the dust lane. (f) The bulge component of the best-fit model. (g) The edge-on disk component of the best-fit model. (h) The extended halo component of the best-fit model. (i) The 1D surface brightness profile. The individual components are shown as dashed lines, and the solid line coursing through the data is the sum of the different components. The lower panel shows the residuals of data—model.

providing accurate photometry to within 0.1–0.2 mag, even if the galaxy shape departs from ellipsoid models quite drastically.

Lastly, Figures 18(e) and (f) demonstrate that it is quite feasible to unambiguously disentangle embedded components that have different shapes, using higher order Fourier modes. Despite there being a large number of parameters, it is visually clear based on Figures 18(e) and (f) that parameter degeneracy is not an issue, because the shapes of the components are quite different. In part, this is possible because of the way Fourier modes are implemented in GALFIT: the profile function is preserved in every direction radially from the peak, even in situations where the shape is irregular, as in Figure 18(e).

7.2. GEMS Edge-on Galaxy

This edge-on galaxy (Figure 19, Table 2) comes from the Galaxy Evolution from Morphology and SED (GEMS; Rix et al. 2004) project, which is an *HST* imaging survey of the *Chandra* Deep Field-South. Belying a benign morphological appearance is a dust lane (Figure 19(e)) that courses through the center, complicating the traditional ellipsoid fitting technique.

The analysis of even this simple object can be quite involved. The best-fitting model involves three components: a fairly compact bulge, an edge-on disk component, and a puffy stellar halo enveloping both. Since the halo component is more luminous than the bulge component, a two-component model fit would naturally ascribe the halo component to the bulge, despite there being a distinctly rounder component at the center. Like the previous example, each of the three components (Figures 19(f)–(h)) is modified by Fourier modes. Furthermore, the best fit includes an actual model for the dust lane (component 4, Table 2). The dust lane is modeled by an inner truncation function as discussed in Section 5.

A truncation model is shown as a model "component" in the fit; it is unique because it is not a light profile model, and one cannot generate an image to see what it looks like. Instead, its influence is to be seen on all the light profile models (i.e., components 1–3; Figures 19(f)–(h)), where it reduces the light by the same fraction for all components. In every other way, the truncation function behaves exactly like a light profile model: it can have its own centroid (or not), and it can be modified by Fourier modes, as shown in Table 2. The benefit of using a single truncation model for all three light profile models is not only to reduce the degrees of freedom, but it is also physically motivated because foreground dust attenuates all background light sources

Table 2
GEMS Disk Galaxy Fitting Results

Parameter	#	– sersic2 – / fourier	Δx ($''$)	Δy ($''$)	mag/arcsec^2	r_e ($''$)	n	q	$\theta_{\rm P.A.}$ (deg)	Comments
			...	mode: ampl. & phase (deg)		mode: ampl. & phase (deg)		mode: ampl. & phase (deg)		
	#	– radial –	Δx ($''$)	Δy ($''$)	...	$r_{\rm break}$ ($''$)	$\Delta r_{\rm soft}$	q	$\theta_{\rm P.A.}$ (deg)	
Best	1	– sersic2 / –	0.00	0.00	19.80	0.40	1.60	0.72	44.00	Trunc. by comp.
fit			0.00	0.00	0.01	0.00	0.01	0.00	0.16	inner: 4
		fourier	...	1: −0.04	1: −92.16	3: −0.00	3: −51.36	4: 0.03	4: −6.61	
			...	1: 0.00	1: 3.23	3: 0.00	3: 30.65	4: 0.00	4: 0.53	
		fourier	...	5: −0.01	5: −5.74	6: 0.01	6: −7.31	...	...	
			...	5: 0.00	5: 2.35	6: 0.00	6: 1.74	...	...	
	2	– sersic2 / –	{0.00}	{0.00}	22.19	2.29	0.85	0.31	41.30	Trunc. by comp.
			{0.00}	{0.00}	0.02	0.01	0.01	0.00	0.03	inner: 4
		fourier	...	1: −0.04	1: −24.97	3: 0.02	3: 26.37	4: −0.02	4: −0.04	
			...	1: 0.00	1: 1.82	3: 0.00	3: 1.03	4: 0.00	4: 0.79	
		fourier	...	5: 0.00	5: 6.19	6: −0.01	6: 6.62	...	...	
			...	5: 0.00	5: 5.63	6: 0.00	6: 1.35	...	...	
	3	– sersic2 / –	{0.00}	{0.00}	23.92	4.45	1.08	0.49	41.06	Trunc. by comp.
			{0.00}	{0.00}	0.03	0.05	0.02	0.00	0.10	inner: 4
		fourier	...	1: 0.04	1: 4.59	3: 0.01	3: −3.37	4: −0.01	4: 40.55	
			...	1: 0.00	1: 1.16	3: 0.00	3: 1.99	4: 0.00	4: 3.94	
		fourier	...	5: 0.01	5: −7.19	6: −0.01	6: −3.25	...	...	
			...	5: 0.00	5: 1.40	6: 0.00	6: 0.73	...	...	
	4	– radial –	0.02	−0.14	...	1.48	1.48	0.09	41.38	Truncates comp.
			0.00	0.00	...	0.01	0.02	0.00	0.05	inner: 1 2 3
		fourier	...	1: −0.12	1: −156.83	3: 0.10	3: −20.62	4: 0.19	4: 9.20	
			...	1: 0.00	1: 1.23	3: 0.00	3: 0.52	4: 0.00	4: 0.15	
		fourier	...	5: 0.10	5: 2.17	6: 0.14	6: 6.62	...	...	
			...	5: 0.00	5: 0.19	6: 0.00	6: 0.10	...	...	
		merit	$\chi^2 = 1474348.38$		$N_{\rm dof} = 1435846$		$N_{\rm free} = 64$	$\chi^2{}_\nu = 1.03$		
Tradit.	1	– sersic2 –	0.00	0.00	19.98	0.38	1.32	0.74	42.75	
ellipsoid			0.00	0.00	0.00	0.00	0.01	0.00	0.31	
model	2	– sersic2 –	{0.00}	{0.00}	22.78	2.57	0.85	0.25	41.21	
with			{0.00}	{0.00}	0.03	0.02	0.01	0.00	0.06	
dust	3	– sersic2 –	{0.00}	{0.00}	23.12	3.34	1.77	0.49	41.30	
masking			{0.00}	{0.00}	0.04	0.04	0.03	0.00	0.08	
		merit	$\chi^2 = 1478767.62$		$N_{\rm dof} = 1434511$		$N_{\rm free} = 18$	$\chi^2{}_\nu = 1.03$		

Notes. Best-fitting parameters for an edge-on disk galaxy in GEMS. See Table 1 for details. The curly braces ({...}) around parameters indicate that they are coupled relative to the first component. Note that the flux amplitude of *sersic2* is normalized to the surface brightness at $r_{\rm e}$, as defined in Equation (32). The "*Best fit*" parameters (top section) correspond to panel (b) in Figure 19, "*Traditional ellipsoid model*" parameters (bottom section) produce residuals shown in panel (c), and the model is not shown.

by an equal fractional amount. Nevertheless, if desired, it is also possible to allow each component to be attenuated differently.

This example also demonstrates how the result of the analysis depends on the input prior of the model. In the fit using traditional ellipsoid parameters, a mask is used to minimize the effect of the dust on the analysis. Yet, the effects cannot be completely removed. As shown in Table 2, the inclusion of the truncation model can significantly affect the structural parameters: the surface brightnesses can differ by 0.8 mag arcsec^{-2}, and the sizes by 10%–20%, even in this seemingly uncomplicated situation. Moreover, the differences far surpass the statistical uncertainties shown in Table 2. To the extent that it is not possible to judge which model is more physically correct, both measurements ought to be treated as equally valid. In that situation, the uncertainties, due entirely to model assumptions, are roughly ~ 0.4 mag in surface brightness and $\sim 10\%$ in size.

7.3. Arp 147

The *HST*/F814W image of the field Arp 147 contains two ring galaxies (Figure 20, Table 3), one of which has a bulge-like component with a tidally disturbed outer region (Galaxy 1), and the other is a pure ring (Galaxy 2). The best-fitting model for Galaxy 2 is a single-component ring, modified by Fourier modes, as seen in Figure 20(b), whereas Galaxy 1 requires two ring components, a bulge, and an inner fine-structure component (Figures 20(e)–(h)). The fine-structure component of Galaxy 1 can easily be seen in the surface brightness profile as an upturn within $r = 0\farcs2$ of Figure 20(i, left). In addition, the tidal component is slightly bent, which is modeled elegantly using the bending modes of Equation (27). As in the case of a dust lane, the ring model comes about by truncating the inner region of a pure Sérsic profile (see Section 5. The only difference here is that the truncation radii are a larger fraction of the galaxy size. Whereas for the edge-on galaxy, it makes more sense to normalize the flux at the effective radius (Equation (32)), for ring galaxies, normalizing the flux at the break radius (Equation (33)) is more intuitive, because it is closer to the peak of the profile model. In fact, the peak of the ring is about half-way between $r_{\rm break}$ and $r_{\rm break} + \Delta r_{\rm soft}$, but the exact location depends on the profile type.

It is again instructive to compare a traditional fit using simple Sérsic ellipsoid models (Table 3, bottom) with more sophisticated analysis (Table 3, top). In terms of the total flux for Galaxy 1, the magnitude of the most sophisticated model

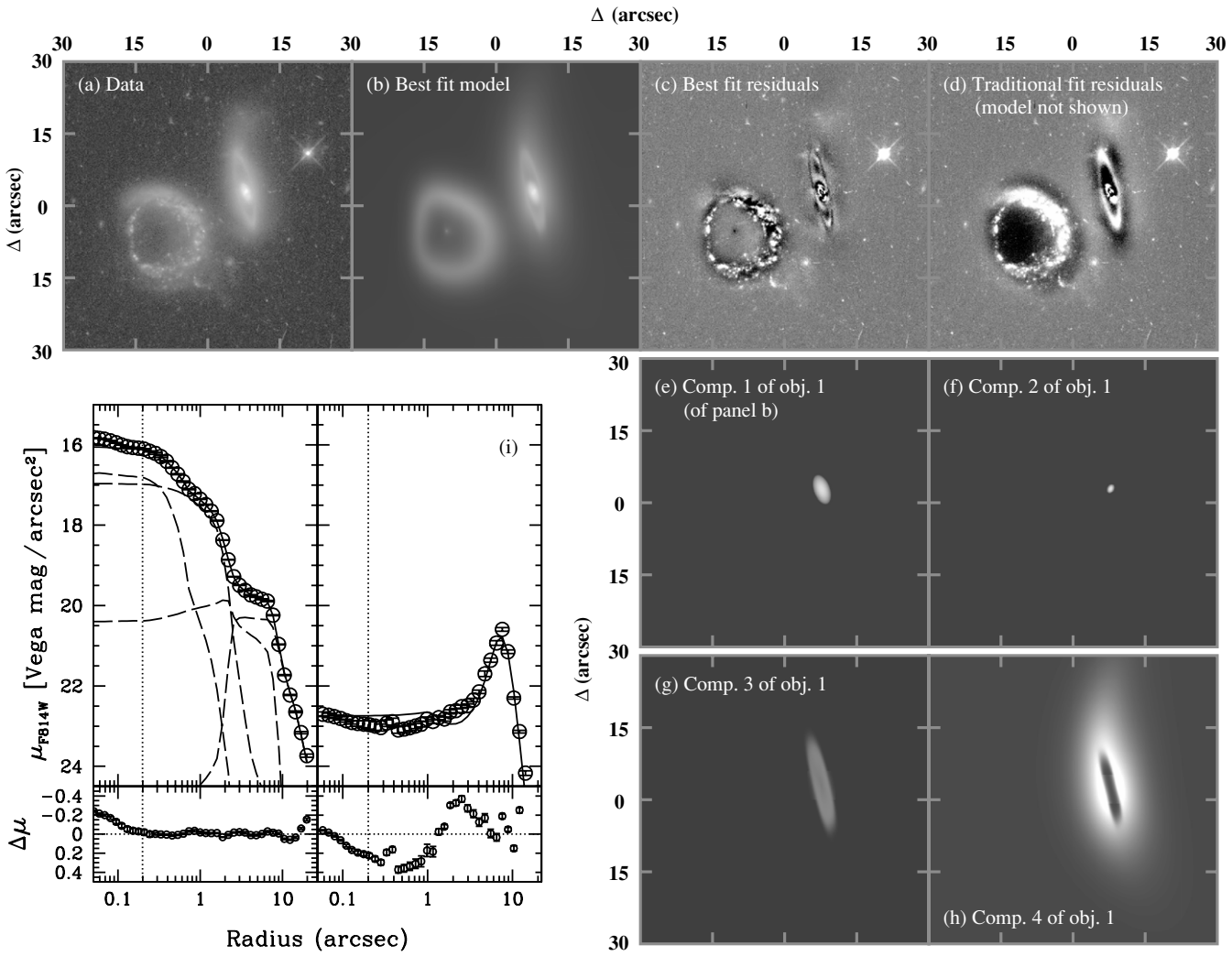

Figure 20. Detailed analysis of Arp 147. (a) Original data. (b) Best Sérsic profile fits of the two galaxies, all with Fourier modes, corresponding to the parameters shown in Table 3. (c) Best-fit residuals. (d) The fit residuals using traditional, i.e., axisymmetric ellipsoidal model components. (e) The bulge component of the right-hand galaxy in panel (b). (f) The inner fine-structure component of the best-fit model. (g) The ring component of the best-fit model. (h) The extended tidal-feature-like component of the best-fit model. (i) The 1D surface brightness profile of the two galaxies. The individual components are shown as dashed lines, and the solid line coursing through the data is the sum of the different components. The lower panel shows the residuals of data–model.

is $m = 14.18$, compared to $m = 14.32$ for a model based on classical ellipsoids. Interestingly, a single-component fit (not shown) to Galaxy 1 yields a magnitude of $m = 14.15$. For Galaxy 2, we know from the outset that classical ellipsoid models are entirely inappropriate to use. Yet, despite every reason to believe that the photometry would be inaccurate, we find that the total flux of the traditional ellipsoid fit is only 0.2 mag different from the most realistic ring model. These two examples show once again that a single-component Sérsic ellipsoid fit to complicated galaxies can produce quite accurate measurement of the total flux.

It is sometimes desirable to conduct B/D decompositions, and Galaxy 1 is an ideal candidate to conduct a comparison. In the traditional ellipsoid model (Table 3, bottom), the B/D ratio is 0.65. The more sophisticated model (Table 3, top) requires summing the ring+tidal feature components to obtain the disk component, which yields 14.65 mag, thus a B/D ratio of 0.54. In this situation, most of the differences arise from measuring the disk component, which differs by 0.2 mag, whereas the bulge component is quite robust, with a difference of only 0.01 mag.

It is also of interest to understand how the structural parameters are affected by different model choices, in particular for the ring Galaxy 2. Whereas the effective radius for the ring model is only 0.″78, for the ellipsoid model it is 8.″28. This is understandable, bearing in mind that the ring has a radius of nearly 8″. To a classical Sérsic profile, the galaxy appears to have a very flat (in fact, a deficit) core, which leads to a low Sérsic index of $n = 0.12$. As most of the flux is at 8″, beyond which the ring flux quickly fades, the ring radius is closely related to the effective radius for a classical Sérsic model. For the inner-truncated ring model (component 7), however, the physical size of the ring is captured by the break radius $r_{\rm break}$ parameter, whereas the r_e term no longer has the classical meaning of the effective radius (i.e., half the light is within r_e). Instead, r_e for component 7 is essentially an exponentially declining scale-length parameter, given by Equation (33). As the flux dies away quickly beyond the peak, as shown in Figure 20(i), the scale length r_e for the ring model must therefore be quite small. The differences in the r_e parameter between the traditional model and the truncated model are therefore only due to

Table 3
Arp 147 Fitting Results

Parameter	#	– sersic –	Δx ($''$)	Δy ($''$)	mag	r_e ($''$)	n	q	$\theta_{\rm P.A.}$ (deg)	Comments
	#	– sersic3 –	Δx ($''$)	Δy ($''$)	mag/arcsec^2	r_e ($''$)	n	q	$\theta_{\rm P.A.}$ (deg)	
		fourier	...	mode: ampl. & phase (deg)		mode: ampl. & phase (deg)		mode: ampl. & phase (deg)		
		bending	...	mode: amplitude ($''$)		mode: amplitude ($''$)		mode: amplitude ($''$)		
	#	– radial –	...	...	...	$r_{\rm break}$ ($''$)	$\Delta r_{\rm soft}$	q	$\theta_{\rm P.A.}$ (deg)	
Galaxy 1	1	– sersic –	0.00	0.00	15.49	1.26	0.47	0.50	194.70	Bulge
			0.00	0.00	0.00	0.00	0.00	0.00	0.05	Inner fine
	2	– sersic –	0.07	0.13	17.39	0.35	0.43	0.60	150.75	structure
			0.00	0.00	0.01	0.00	0.01	0.00	0.39	
	3	– sersic3 / –	−0.08	0.33	23.84	1.21	0.96	0.18	187.42	Trunc. by comp.
			0.01	0.03	0.02	0.02	0.01	0.00	0.03	inner: 5 (ring)
		fourier	...	1: 0.03	1: 49.11	3: 0.02	3: 15.69	4: 0.04	4: 4.24	
			...	1: 0.00	1: 9.08	3: 0.00	3: 1.04	4: 0.00	4: 0.45	
	4	– sersic3 / –	0.09	−0.34	22.04	3.81	1.94	0.42	184.08	Trunc. by comp.
			0.01	0.02	0.01	0.04	0.03	0.00	0.04	inner: 5 (Tidal
		fourier	...	1: 0.16	1: 21.49	3: 0.09	3: 18.36	4: −0.01	4: 16.13	feature)
			...	1: 0.00	1: 0.82	3: 0.00	3: 0.17	4: 0.00	4: 1.55	
		bending	...	2: −0.14	...	...	...	...	...	
			...	2: 0.00	...	...	...	...	...	
	5	– radial –	...	...	...	10.94	6.00	0.18	187.61	Truncates comp.
			...	...	...	0.02	0.06	0.00	0.03	inner: 3 4
		fourier	...	1: 0.05	1: 39.00	3: 0.02	3: 19.88	4: 0.04	4: 3.88	
			...	1: 0.00	1: 4.97	3: 0.00	3: 1.18	4: 0.00	4: 0.39	
Galaxy 2	6	– sersic3 / –	−18.29	−7.93	22.14	0.78	1.85	0.79	187.91	Trunc. by comp.
			0.01	0.01	0.00	0.01	0.01	0.00	0.12	inner: 7 (Ring)
		fourier	...	1: 0.23	1: −113.97	3: 0.07	3: 15.27	4: −0.02	4: 23.33	$\rm mag_{tot} = 14.90$
			...	1: 0.00	1: 0.53	3: 0.00	3: 0.12	4: 0.00	4: 0.39	
	7	– radial –	...	...	...	10.77	6.08	0.82	195.16	Truncates comp.
			...	...	...	0.01	0.01	0.00	0.19	inner: 6
		fourier	...	1: 0.17	1: −149.22	3: 0.07	3: 4.98	4: 0.02	4: −31.52	
			...	1: 0.00	1: 0.99	3: 0.00	3: 0.17	4: 0.00	4: 0.38	
		merit	$\chi^2 = 714735.38$		$N_{\rm dof} = 357760$		$N_{\rm free} = 77$	$\chi^2_\nu = 2.00$		
Tradit.	1	– sersic –	0.00	0.00	15.33	1.07	0.90	0.62	193.49	Bulge
ellipsoid			0.00	0.00	0.00	0.00	0.00	0.00	0.11	
model	2	– sersic –	−0.12	0.55	14.86	6.63	0.43	0.34	184.20	Disk
			0.00	0.01	0.00	0.01	0.00	0.00	0.04	
Galaxy 2	3	– sersic –	−15.61	−8.66	15.09	8.28	0.12	0.80	201.65	Ring
			0.01	0.01	0.00	0.01	0.00	0.00	0.29	galaxy
		merit	$\chi^2 = 1435193.25$		$N_{\rm dof} = 357813$		$N_{\rm free} = 24$	$\chi^2_\nu = 4.01$		

Notes. Best-fitting parameters for Arp 147. See Table 1 for details. Note that the flux amplitude of *sersic3* is normalized to the surface brightness at $r_{\rm break}$, as defined in Equation (33), whereas *sersic* magnitude means the total flux. The "*Best fit*" parameters (top section) correspond to panel (b) in Figure 20, "*Traditional ellipsoid model*" parameters (bottom section) produce residuals shown in panel (d), and the model is not shown. The free parameters for the sky are not listed.

definitions, and not due to systematic or random measurement uncertainties.

7.4. M51

The classical Whirlpool galaxy is a beautiful system where a grand-design spiral, M51A, is interacting with another spiral, M51B (Figure 21, Table 4). In addition to there being obvious spiral structures for both galaxies, there are large tidal disturbances that emerge from M51B, as seen in the Sloan Digital Sky Survey (SDSS) *r*-band image provided by D. Finkbeiner. Because they are closely overlapping, a desirable goal is to deblend M51A and B, as well as to model the spiral and tidal structures, simultaneously.

As with previous examples, we fit this galaxy using both the most sophisticated analysis (Table 4, top) in our toolbox, and comparing the results to the traditional axisymmetric ellipsoids (Table 4, bottom) analysis. The traditional analysis requires two components each, in order to decompose a galaxy ostensibly into a bulge and a disk. The reduction in χ^2_ν between the two methods is modest, because most of the residuals come from high-frequency star-forming regions that are not removed by models which are fundamentally smooth, despite being modified by radial Fourier modes and spiral rotations.

In the most detailed analysis of M51A, we use two spiral arm components and two components for the bulge. There is actually not a strong need to use two components for the bulge except to better capture the detailed profile shape, which has an inflection at $r \approx 0.'4$, as seen in Figure 21(i). On the other hand, the use of two spiral components is necessary because the spiral arm has a "kink" in the rotation that cannot be created by using a single smooth rotation function. The spiral structures are modified by Fourier modes to create both a slight lopsidedness and other subtle features. Because there are more degrees of freedom in a two-arm spiral, the higher order Fourier modes also can "see" detailed structures, like the reverse flaring of the spiral structure in Figure 21(f).

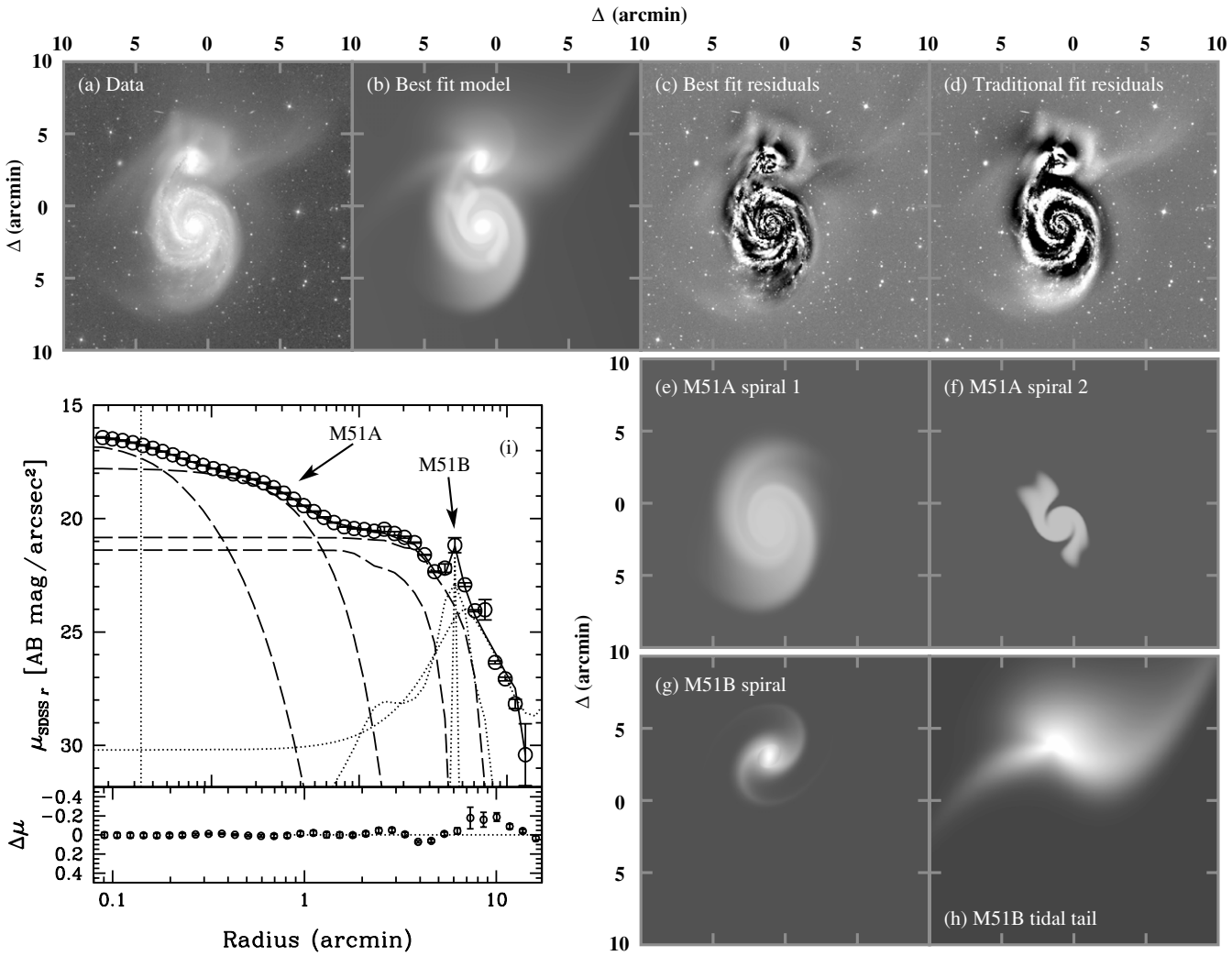

Figure 21. Detailed analysis of M51. (a) Original data. (b) Best Sérsic profile fits of the M51A and B, all with Fourier modes, corresponding to the parameters shown in Table 4. (c) Best-fit residuals. (d) The fit residuals using traditional, axisymmetric, ellipsoidal model components. (e) The extended grand-design spiral component of M51A model in panel (b). (f) The inner fine-structure spiral component of the best-fit model. (g) The spiral component of M51B. (h) The extended tidal-feature-like component of M51B, using simultaneous bending and Fourier modes. A bulge component is present but not shown in the figures of M51A and B. (i) The 1D surface brightness profile of the two galaxies. The individual components are shown as dashed lines, and the solid line coursing through the data is the sum of the different components. The lower panel shows the residuals of data–model.

For M51B, we employ three components in the fit, a bulge (component 5 in Table 4, top), a tidal feature component (component 6), and a spiral function (component 7), which model the three most visually striking components. The tidal feature is mostly obtained by using the second and third bending modes of Equation (27), as illustrated in Figure 10. However, bending modes 2 and 3 are symmetric functions, so the high degree of asymmetry comes about because of combined action with the Fourier modes, which is shown to have a high amplitude of 0.23 for the $m = 1$ mode, as well as moderate values for other modes. Incidentally, despite the complexity of the higher order structures, all the parameter values are determined automatically by GALFIT without the need for an user to provide initial guesses (i.e., initially all 0 values) and without tweaking at any point in the analysis (which is hardly feasible anyhow).

For even those who are experienced with detailed parametric fitting, one of the alarming facts about this analysis is that it employs 103 free parameters in the best-fit model. So there are natural concerns about parameter degeneracies. However, as we have discussed in Section 6.5, parameter degeneracies do not arise purely based on the number of free parameters, but rather on the types of parameters involved. The availability of spatial information in 2D provides one of the most important ways to break parameter degeneracies. We see this explicitly in Figures 21(e)–(h), where there is little evidence that the subcomponents for M51A are strongly influenced by M51B, and vice versa. Furthermore, within each galaxy, the subcomponents are so different in shape, both qualitatively and quantitatively, that the amount of cross talk between them is also not significant. Therefore, despite the extreme complexity of this system, and the use of 103 free parameters, we find that degeneracies between the parameters are not an issue. Or, if they exist, they do so at a low enough level that they do not significantly affect the main parameters of interest, like the luminosity of the subcomponents, or the profile shapes and sizes.

There *are*, however, seemingly degenerate conditions that have little to do with parameter coupling. Instead, these are attributed to the fact that M51 has many non-smooth structural features, caused by dust lanes, star-forming regions, tidal disturbances, and so forth. Such spatially localized features, if strong enough, can influence GALFIT to "lock" on to them

Table 4
M51 Fitting Results

Parameter	#	– sersic –	Δx (′)	Δy (′)	mag	r_e (′)	n	q	$\theta_{\rm P.A.}$ (deg)	Comments
		power	...	$r_{\rm in}$ (′)	$r_{\rm out}$ (′)	$\theta_{\rm rot}$ (deg)	α	$\theta_{\rm incl}$ (deg)	$\theta_{\rm sky}$ (deg)	
		fourier	...	mode: ampl. & phase (deg)		mode: ampl. & phase (deg)		mode: ampl. & phase (deg)		
		bending	...	mode: amplitude (′)		mode: amplitude (′)		mode: amplitude (′)		
Best	1	– sersic –	0.00	0.00	13.09	0.04	1.18	0.91	−15.25	Compound
fit			0.00	0.00	0.04	0.00	0.04	0.01	4.74	bulge
	2	– sersic –	{0.00}	{0.00}	10.49	0.26	0.67	0.88	−65.31	Compound
M51A			{0.00}	{0.00}	0.00	0.00	0.01	0.00	0.66	bulge
	3	– sersic –	{0.00}	{0.00}	8.50	2.78	0.35	0.75	−87.22	Compound
			{0.00}	{0.00}	0.00	0.00	0.00	0.00	39.53	spiral
		power	...	−1.29	4.28	−718.11	0.29	40.42	−82.20	
			...	0.20	0.03	41.39	0.02	0.05	0.10	
		fourier	...	1: −0.07	1: 109.10	3: 0.03	3: 4.07	4: 0.02	4: −36.57	
			...	1: 0.00	1: 0.44	3: 0.00	3: 0.43	4: 0.00	4: 0.35	
		fourier	...	5: 0.02	5: 24.34	...	...	...	...	
			...	5: 0.00	5: 0.32	...	...	...	...	
	4	– sersic –	{0.00}	{0.00}	10.06	1.88	0.14	0.39	5.45	Compound
			{0.00}	{0.00}	0.00	0.00	0.00	0.00	4190.51	spiral
		power	...	0.66	2.34	−172.67	−0.11	−0.01	15.58	
			...	0.02	0.01	3.51	0.01	1100.08	4190.50	
		fourier	...	1: −0.15	1: 25.39	3: 0.02	3: −32.12	4: 0.15	4: 8.38	
			...	1: 0.00	1: 0.62	3: 0.00	3: 1.50	4: 0.00	4: 0.19	
		fourier	...	5: 0.02	5: −4.02	...	...	...	...	
			...	5: 0.00	5: 0.82	...	...	...	...	
M51B	5	– sersic –	−0.19	4.44	12.06	0.05	0.89	0.62	−72.22	Compound
			0.00	0.00	0.01	0.00	0.01	0.00	0.38	bulge
	6	– sersic –	−0.16	4.43	11.93	0.18	1.06	0.81	−2.79	Compound
			0.00	0.00	0.02	0.00	0.03	0.01	1.45	bulge
	7	– sersic –	−0.45	5.19	9.93	2.51	[1.00]	0.62	−96.19	Tidal
			0.01	0.01	0.00	0.01	...	0.00	0.36	structure
		bending	...	2: 0.03	3: −0.15	...	...	...	...	
			...	2: 0.02	3: 0.00	...	...	...	...	
		fourier	...	1: 0.34	1: 17.20	3: −0.25	3: 32.55	4: 0.14	4: −3.73	
			...	1: 0.00	1: 0.81	3: 0.00	3: 0.40	4: 0.00	4: 0.43	
		fourier	...	5: 0.03	5: 7.32	...	...	...	...	
			...	5: 0.00	5: 1.16	...	...	...	...	
	8	– sersic –	−0.10	4.52	10.20	0.90	0.72	0.58	−46.52	Bar and
			0.00	0.00	0.00	0.00	0.00	0.00	0.56	spiral
		power	...	0.88	1.08	46.34	1.60	42.29	52.50	
			...	0.00	0.00	0.66	0.01	0.16	0.25	
		fourier	...	1: 0.07	1: 103.72	3: 0.05	3: 28.79	4: 0.01	4: −0.11	
			...	1: 0.00	1: 1.59	3: 0.00	3: 0.52	4: 0.00	4: 4.25	
		fourier	...	5: 0.01	5: 23.12	...	...	...	...	
			...	5: 0.00	5: 1.09	...	...	...	...	
		merit	$\chi^2 = 34279512.00$		$N_{\rm dof} = 632434$		$N_{\rm free} = 104$	$\chi^2{}_\nu = 54.20$		
Trad.	1	– sersic –	0.00	0.00	10.05	0.33	1.75	0.85	−62.09	
ellipsoid			0.00	0.00	0.00	0.00	0.01	0.00	0.55	
model	2	– sersic –	−0.06	−0.13	8.47	2.21	0.33	0.75	26.69	
M51A			0.00	0.00	0.00	0.00	0.00	0.00	0.13	
M51B	3	– sersic –	−0.18	4.40	8.93	2.54	8.02	0.92	−44.73	
			0.00	0.00	0.03	0.11	0.09	0.00	1.24	
	4	– sersic –	−0.04	4.90	10.66	1.45	1.66	0.57	71.33	
			0.00	0.00	0.02	0.02	0.02	0.00	0.42	
		merit	$\chi^2 = 42126720.00$		$N_{\rm dof} = 632507$		$N_{\rm free} = 31$	$\chi^2{}_\nu = 66.60$		

Notes. Best-fitting parameters for M51. See Table 3 for details. The "*Best fit*" parameters (top section) correspond to panel (b) in Figure 21, "*Traditional ellipsoid model*" parameters (bottom section) produce residuals shown in panel (d), and the model is not shown. The free parameters for the sky are not listed. The parameter in square brackets, [...], is held constant in the fit. The curly braces ({...}) around parameters indicate that they are coupled relative to the first component.

if the initial conditions happened to be sufficiently close. The consequences appear as degeneracies when, in fact, there are many small local minima solutions. This graininess in the χ^2 terrain introduces slight perturbations to the models, and may even cause fairly large shape differences in the final solutions. However, to a large extent, it rarely affects the main parameters of interest, such as the luminosity of a particular component or its size, which are determined by much more global features than the nuisances of local fluctuations to which higher order parameters are more sensitive.

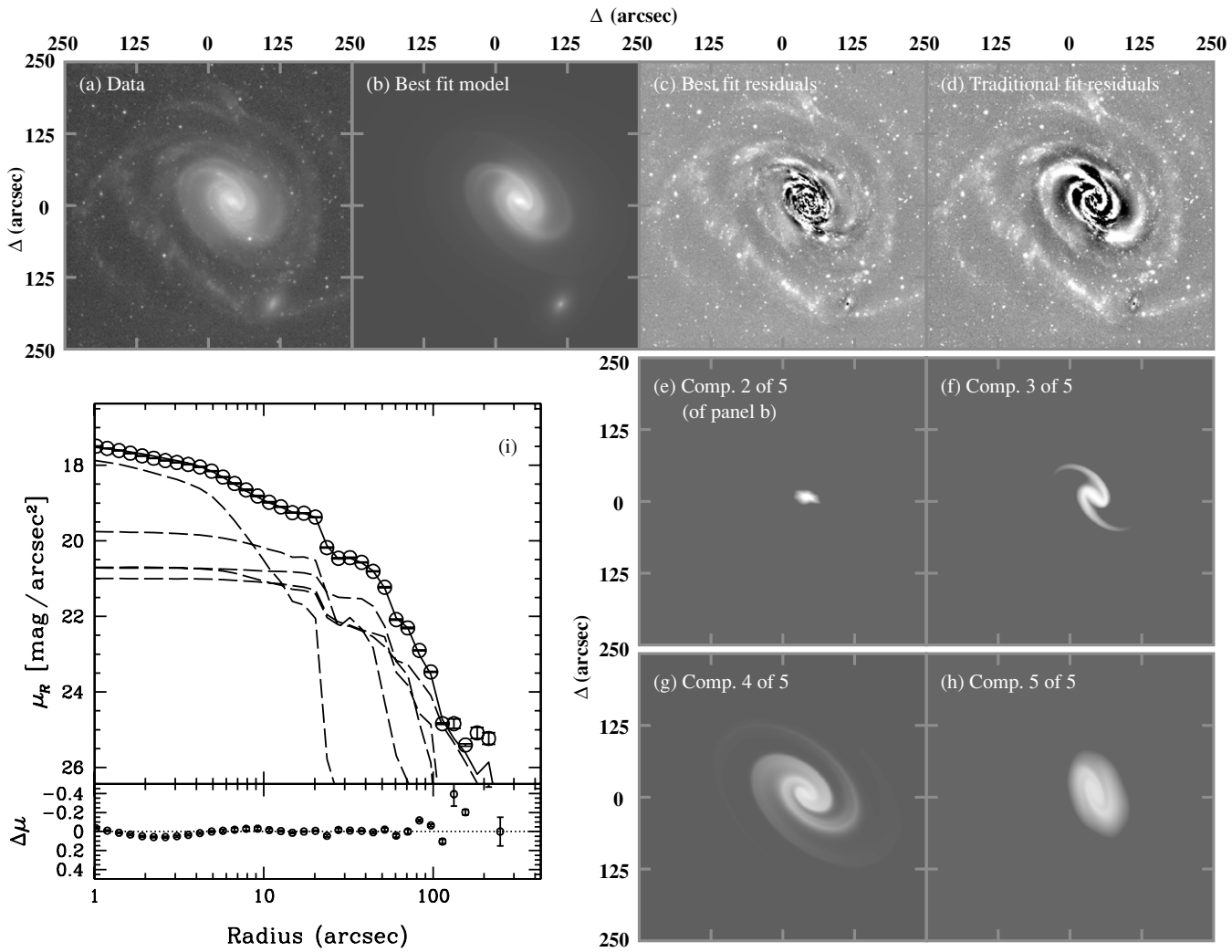

Figure 22. Detailed analysis of NGC 289 from CINGS. (a) Original data. (b) Best Sérsic profile fits with spiral rotation functions and Fourier modes, corresponding to the parameters shown in Table 5. (c) Best-fit residuals. (d) The fit residuals using traditional, axisymmetric, ellipsoidal model components. (e) The fine details of the inner bar structure of panel (b). (f) Spiral component 1 of 3 of the best-fit model. (g) The spiral component 2 of 3. (h) The spiral component 3 of 3. A bulge component is present but not shown in the figures. (i) The 1D surface brightness profile of the galaxy. The individual components are shown as dashed lines, and the solid line coursing through the data is the sum of the different components. The lower panel shows the residuals of data –model.

To gain some intuitive insight into the effects of complex analysis, it is instructive to compare simple and complex methods with regard to global and subcomponent properties. In terms of the total luminosity, here we find excellent agreement between sophisticated and traditional analysis, respectively, of $m_r = 8.24$ versus $m_r = 8.25$ for M51A, and $m_r = 8.80$ versus $m_r = 8.73$ for M51B. While this level of agreement may at first seem surprising, it is expected given the basic premise of least-squares minimization. In fact, even a single-component fit to M51A yields $m_r = 8.0$, and for M51B $m_r = 9.0$, which are both quite close to the overall best-fit models, despite the complications in the image. The main reason for the discrepancy here is the uncertainty in the sky, due to there being a large gradient. This fundamentally sets the limit on the accuracy of the photometry to perhaps no better than 0.1 to 0.2 mag, independent of the analysis method.

The most sensitive benchmark for understanding differences in the analysis is in detailed decompositions. Here we compare the B/D decomposition results. In the traditional ellipsoid analysis, we find a B/D ratio of 0.23 for M51A and 4.9 for M51B. The large B/D ratio for M51B is clearly unphysical, and is driven by the large Sérsic index ($n = 8.0$) of the bulge component, which is increased to accommodate the flux in the outskirts due to tidal features. In the most detailed analysis, the B/D ratio for M51A is 0.16, whereas for M51B it is merely 0.17. Examining the bulge of M51A more closely, we find that the detailed analysis yields a total flux of 10.38 mag, whereas the traditional analysis extracts a brighter bulge of 10.05 mag. The differences come from the fact that the light of the inner spiral is in part driving up the Sérsic index of the bulge when it is not properly accounted. It is probably safe to conclude that a magnitude of 10.05 is a firm upper limit to the bulge luminosity.

Finally, it is worthwhile to compare how the disk parameters differ between the analyses to gain an understanding for how coordinate rotation affects the interpretation of the parameters for the spiral models. From Table 4, we find that the Sérsic indices of the simple and complex models are essentially identical for M51A, at $n \approx 0.33$. The interpretation for M51B is more complicated, because the "disk" in an ellipsoidal model is not qualitatively the same structure as the spiral analysis. In fact, it is necessary to hold the Sérsic index of the tidal component 6 fixed in the analysis. Nevertheless, there are clearly quantitative differences in that the simple analysis is larger by 55% in n. With regard to the effective radius, the traditional analysis of

Table 5
NGC 289 Fitting Results

Parameter	#	– sersic –	Δx ($''$)	Δy ($''$)	mag	r_e ($''$)	n	q	$\theta_{\rm P.A.}$ (deg)	Comments
		power	...	$r_{\rm in}$ ($''$)	$r_{\rm out}$ ($''$)	$\theta_{\rm rot}$ (deg)	α	$\theta_{\rm incl}$ (deg)	$\theta_{\rm sky}$ (deg)	
		fourier	...	mode: ampl. & phase (deg)		mode: ampl. & phase (deg)		mode: ampl. & phase (deg)		
Best	1	– sersic –	0.00	0.00	11.69	64.01	1.72	0.78	61.27	Bulge
fit			0.09	0.10	0.01	0.75	0.03	0.00	0.43	
	2	– sersic –	−2.63	−1.92	13.27	6.05	1.02	0.51	77.83	Inner
NGC 289			0.02	0.01	0.01	0.04	0.01	0.00	0.29	bar
		fourier	...	1: 0.10	1: 63.87	3: −0.05	3: −4.23	4: −0.05	4: −20.77	
			...	1: 0.01	1: 4.87	3: 0.00	3: 0.92	4: 0.00	4: 0.95	
		fourier	...	5: 0.03	5: 4.62	6: 0.06	6: −2.09	...	...	
			...	5: 0.00	5: 1.32	6: 0.00	6: 0.61	...	...	
	3	– sersic –	−2.25	−2.77	12.30	32.86	0.54	0.32	−85.94	Spiral
			0.02	0.02	0.01	0.15	0.00	0.00	0.53	comp. 1
		power	...	19.23	34.40	85.51	1.48	52.11	136.18	
			...	0.14	0.14	0.94	0.02	0.08	0.10	
		fourier	...	1: 0.14	1: −97.28	3: −0.05	3: −8.55	4: 0.02	4: 3.41	
			...	1: 0.00	1: 0.74	3: 0.00	3: 1.13	4: 0.00	4: 2.09	
		fourier	...	5: 0.02	5: −3.77	6: 0.01	6: 10.09	...	...	
			...	5: 0.00	5: 0.99	6: 0.00	6: 3.36	...	...	
	4	– sersic –	−4.54	−4.10	12.13	52.28	0.74	0.56	−32.85	Spiral
			0.04	0.03	0.01	0.22	0.01	0.00	28.48	comp. 2
		power	...	−26.32	71.31	450.01	0.77	53.30	140.24	
			...	4.45	0.59	25.64	0.06	0.05	0.07	
		fourier	...	1: −0.12	1: 84.16	3: 0.06	3: 32.07	4: −0.06	4: −30.37	
			...	1: 0.00	1: 0.64	3: 0.00	3: 0.45	4: 0.00	4: 0.38	
		fourier	...	5: 0.04	5: −6.47	6: 0.02	6: −20.35	...	...	
			...	5: 0.00	5: 0.32	6: 0.00	6: 0.81	...	...	
	5	– sersic –	−2.40	−1.90	11.82	50.67	0.46	0.68	−45.45	Spiral
			0.04	0.04	0.00	0.30	0.00	0.00	35.81	comp. 3
		power	...	−9.09	75.87	411.91	−0.04	64.81	112.75	
			...	4.42	0.69	36.56	0.01	0.13	0.09	
		fourier	...	1: −0.11	1: −33.85	3: 0.01	3: 1.93	4: −0.00	4: 9.85	
			...	1: 0.00	1: 1.08	3: 0.00	3: 3.10	4: 0.00	4: 6.71	
		fourier	...	5: 0.00	5: −16.26	6: 0.02	6: −6.02	...	...	
			...	5: 0.00	5: 10.08	6: 0.00	6: 0.58	...	...	
Neighbor	6	– sersic –	67.90	−181.06	14.69	20.03	1.93	0.72	−34.31	
galaxy			0.04	0.05	0.01	0.34	0.03	0.01	0.99	
		merit	$\chi^2 = 158680.39$		$N_{\rm dof} = 150419$		$N_{\rm free} = 103$	${\chi^2}_\nu = 1.05$		
Tradit.	1	– sersic –	0.00	0.00	11.03	41.90	1.62	0.74	54.96	"bulge"?
ellipsoid			0.04	0.03	0.01	0.33	0.01	0.00	0.21	
model	2	– sersic –	2.01	−3.52	11.69	36.98	0.29	0.55	23.85	disk
			0.04	0.05	0.01	0.06	0.00	0.00	0.12	
	3	– sersic –	0.02	−1.10	12.70	10.83	1.24	0.43	67.37	bar
			0.02	0.01	0.03	0.08	0.01	0.00	0.19	
Neighbor	4	– sersic –	70.60	−179.97	14.71	19.62	1.90	0.72	−34.01	
galaxy			0.04	0.05	0.01	0.34	0.03	0.01	1.11	
		merit	$\chi^2 = 200361.19$		$N_{\rm dof} = 150491$		$N_{\rm free} = 31$	${\chi^2}_\nu = 1.33$		

Notes. Best-fitting parameters for NGC 289. See Table 1 for details. The "*Best fit*" parameters (top section) correspond to panel (b) in Figure 22, "*Traditional ellipsoid model*" parameters (bottom section) produce residuals shown in panel (d), and the model is not shown. The free parameters for the sky are not listed.

M51A finds the disk size to be about 2.′2, which compares favorably with the spiral model size of 2.′8, or a 25% difference. Furthermore, the disk magnitudes for M51A differ only by 0.03 mag between simple and complex.

These comparisons therefore demonstrate that despite the complex analysis being much more realistic looking, fundamentally the meaning of the structural parameters (size, luminosity, concentration index) is unchanged from the original definition, even in the situation of spiral components. This is a useful fact because our prior intuitions, honed on fitting ellipsoidal models, continue to be applicable. We note that the generally good agreement between detailed and simplistic analysis witnessed here and in previous examples is not entirely coincidental. It so happens because all shapes are fundamentally perturbations of the best-fitting ellipsoidal model, even if the result bears no resemblance to the original ellipse.

7.5. NGC 289

NGC 289 is an SAB(rs)bc galaxy, with a weak bar and a complex inner spiral system (Figure 22, Table 5) that resembles a ring. Upon closer examination, the ring appearance comes about because there exists a bifurcation in the spiral structure that connects up with the opposing spiral arm. Furthermore, the bar is also multi-component, with the inner component oriented at an angle nearly 45° from the strong outer bar.

The best-fit analysis involves three spiral components, an inner and an outer bar component, and a bulge (Table 5, top). All except for the bulge component are modified by five Fourier modes, and are shown in Figures 22(e)–(h). The requirement of components 3 and 4 (Figures 22(f) and (g)) is clear, because they are what form the most striking and intricate patterns in the center, while the requirement of component 5 (Figure 22(h)) is only evident in the residuals, and makes up some of the diffuse light within the inner 60″ region. Although it does not seem like an essential component, the inner bar structure (Figure 22(e)) qualitatively affects the detailed residual pattern at the center, and is therefore included. When all the detailed inner structures are properly accounted for, it is straightforward to infer the bulge component, and assess the uncertainties by varying different parameters of the bulge. Doing so does not affect the inner fine structures because they are sharp and well localized.

Conducting the same decomposition using traditional ellipsoid models (Table 5, bottom), we opted to fit three components, ostensibly to model a bulge, disk, and a bar. The result produces residuals seen in Figure 22(d), revealing the intricate details of the inner spiral system. From the fit, even though the disk and the bar component are sensible, the bulge component is actually fitting a diffuse disk component, which, in retrospect, is that shown in Figure 22(h). Because that inner spiral component is quite luminous, and because there exists a bulge component superposed on top of it, this quasi-bulge model is almost 0.7 mag brighter than that inferred through the detailed modeling above. Adding a fourth ellipsoid model is not possible, because the central spiral residuals are so great that they completely suppress the addition of another component, causing the flux to go to zero.

Once again, comparing the total luminosity between the best-fit model with the ellipsoid fit, we find an excellent agreement of $m = 10.37$ mag versus $m = 10.42$, respectively. For a single-component ellipsoid fit, there is also an excellent agreement of $m = 10.46$, despite the main structural details not being unaccounted.

8. DISCUSSION AND CONCLUSIONS

This study is a proof of concept for how to conduct more realistic image-fitting analysis using purely parametric functions, by breaking free from traditional assumptions about axisymmetry. We introduced several new ideas, including the use of Fourier and bending modes, spiral rotation functions, and truncation functions. These features can be used individually, or combined in arbitrary ways. While these features are individually quite simplistic, used collectively they proliferate a dizzying array of possibilities. Even so, the interpretation of each component remains intuitive, down to the meaning of each fitting parameter. Indeed, the interpretation of the traditional ellipsoidal profile parameters, such as those for the Sérsic function, remains essentially unchanged under modification. We then applied these techniques to five case studies, illustrating that highly complex and intricate structures can be modeled using fully parametric techniques.

There are many practical applications for these techniques. For instance, the Fourier modes are useful for quantifying the average global symmetry of a galaxy, and can easily be automated for galaxy surveys. It is also possible to disentangle bright from faint asymmetries, and to conduct more robust B/D decompositions in some galaxies. It would be useful to quantify how much of the total flux is in a bulge versus the tidally distorted component, which has implications for issues such as late- versus early-stage mergers, or major versus minor mergers.

More than just a presentation of new techniques, one of the main purposes of this study is to highlight a method to more realistically quantify measurement uncertainties in high-S/N images. In galaxy fitting, the most desirable goal will always be to obtain a fit with the lowest χ^2, using the simplest model. In the past, this idea was closely tied to the practice of using one- or two-component ellipsoid models, out of necessity. Simplicity is not necessarily congruent with propriety or reality. This study promotes the notion that simple models can be realistic. It also opens up new possibilities for more detailed analysis depending on the image complexity. However, this possibility is both a blessing and a curse. For, the fact there is not one generic solution for any galaxy leads to the following conundrum in image analysis, but one that illustrates the merit of our approach: *"What model should one adopt, how much detail is enough, and what about degeneracies?"* We have shown that detailed decomposition analysis can be arbitrarily sophisticated. It is for that same reason there is often not a single, unique answer. However, the essential fact, as seen through our examples and other detailed analysis outside of this work, is that the marginal return of adding complexity quickly diminishes. Therefore, the above conundrum is in practice easy to address by conducting analyses of varying sophistication without prejudice, then judging the outcome by taking a clear view of what goal is to be achieved. If different solutions yield the same result for a desired science goal (e.g., bulge luminosity, B/D ratio, average size, total luminosity, etc.), then it does not matter which model one adopts. If they yield different outcomes, then the most realistic analysis ought to be the more true. However, if it is not possible to decide on the correct model, the different results by definition give an estimate of the model-dependent *measurement uncertainty.* This last attribute, rather than being a perceived weakness, is fundamentally that which makes the analysis quantitatively rigorous.

Despite the flexibility allowed by the models, this paper is merely an initial demonstration of concept and leaves many issues unsolved. Currently, the formulation of the spiral rotation function is fairly rigid, and cannot produce arms that wind back onto itself (although that can be approximated using the ring feature in GALFIT). The amount of curvature in the bending modes can only fit arcs and not fuller semi-circles (which can partly be modeled using a lopsided ring). There remains substantial room for future growth in profile types, shape definitions, and toward spatial-spectral decompositions for integral-field data.

C.Y.P. gratefully acknowledges discussions with and suggestions from many people over the course of this work, including Lauren A. MacArthur who greatly improved this manuscript, J. Greene, C. Brasseur, D. McIntosh, J. Hesser, T. Puzia, K. Jahnke, S. Zibetti, E. Bell, A. Barth, E. Laurikainen, M. Barden, B. Häussler, M. Gray, and GALFIT users over the years. We thank the anonymous referee for an expeditious review that improved the discussions. A number of individuals not only very kindly provided us high-quality images, but also granted us permission to analyze and use them for this study, including M. Seigar and A. Barth for IC 4710 and NGC 289 from the Carnegie Irvine Nearby Galaxy Survey, D. Finkbeiner for the SDSS image of M51, J. Caldwell and the GEMS collaboration for the edge-on galaxy from their survey. Several others, including J. Lee, M. Kim, and H. Hernandez, contributed

galaxy images that motivated the development of certain GALFIT features. The various contributions and input from all made the development of this software a greatly enjoyable endeavor, and to whom C.Y.P. is greatly indebted. This work was made possible by the generous financial support of the Herzberg Institute of Astrophysics, National Research Council of Canada, through the Plaskett Fellowship program, by STScI through the Institute/Giacconi Fellowship, and by visitor programs of the Max-Planck-Institut Für Astronomie, operated by the Max-Planck Society of Germany. This research has made use of the NASA/IPAC Extragalactic Database (NED) which is operated by the Jet Propulsion Laboratory, California Institute of Technology, under contract with the National Aeronautics and Space Administration. Based on observations made with the NASA/ESA *Hubble Space Telescope*, and obtained from the Hubble Legacy Archive, which is a collaboration between the Space Telescope Science Institute (STScI/NASA), the Space Telescope European Coordinating Facility (ST-ECF/ESA), and the Canadian Astronomy Data Centre (CADC/NRC/CSA). Funding for the SDSS and SDSS-II has been provided by the Alfred P. Sloan Foundation, the Participating Institutions, the National Science Foundation, the U.S. Department of Energy, the National Aeronautics and Space Administration, the Japanese Monbukagakusho, the Max Planck Society, and the Higher Education Funding Council for England. The SDSS Web site is http://www.sdss.org/. The SDSS is managed by the Astrophysical Research Consortium for the Participating Institutions. The Participating Institutions are the American Museum of Natural History, Astrophysical Institute Potsdam, University of Basel, University of Cambridge, Case Western Reserve University, University of Chicago, Drexel University, Fermilab, the Institute for Advanced Study, the Japan Participation Group, Johns Hopkins University, the Joint Institute for Nuclear Astrophysics, the Kavli Institute for Particle Astrophysics and Cosmology, the Korean Scientist Group, the Chinese Academy of Sciences (LAMOST), Los Alamos National Laboratory, the Max-Planck-Institute for Astronomy (MPIA), the Max-Planck-Institute for Astrophysics (MPA), New Mexico State University, Ohio State University, University of Pittsburgh, University of Portsmouth, Princeton University, the United States Naval Observatory, and the University of Washington.

APPENDIX A

HYPERBOLIC TANGENT ROTATION FUNCTION

The hyperbolic tangent ($\tanh(r_{\rm in}, r_{\rm out}, \theta_{\rm incl}, \theta^{\rm sky}_{\rm P.A.}; r)$) portion of the α-tanh (Equation (28)) and log-tanh (Equation (29)) rotation functions is given by Equation (A5) below. The constant CDEF is defined such that at the mathematical "bar radius" $r_{\rm in}$, the rotation angle θ reaches 20°. This definition is entirely empirical. Figure A1 shows a pure tanh rotation function, where the rotation angle reaches a maximum $\theta_{\rm out}$ near $r = r_{\rm out}$. Beyond $r_{\rm out}$, the rotation angle levels off at $\theta_{\rm out}$. This function is multiplied with either a logarithmic or a power-law function to produce the desired asymptotic rotation behavior seen in more realistic galaxies (see Section 4).

$$\mathrm{CDEF} = 0.23 \quad \text{(constant for "bar" definition)} \tag{A1}$$

$$A = \frac{2 \times \mathrm{CDEF}}{|\theta_{\rm out}| + \mathrm{CDEF}} - 1.00001 \tag{A2}$$

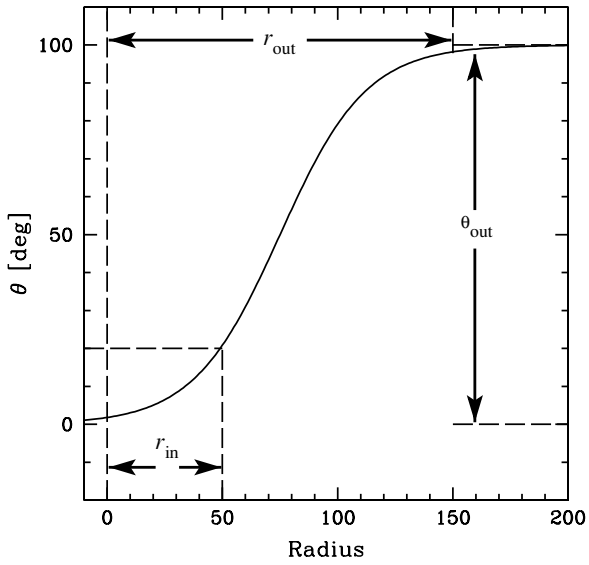

Figure A1. Schematics of a hyperbolic tangent rotation function. $r_{\rm in}$ is the inner radius where the rotation angle reaches 20° relative to the P.A. of the best-fitting ellipse of a component. Below $r_{\rm in}$ the function flattens out to 0°. $r_{\rm out}$ is the outer radius, beyond which the function flattens out to a constant rotation angle, and $\theta_{\rm out}$ is the total amount of rotation out to $r_{\rm out}$.

$$B = \left(2 - \tanh^{-1}(A)\right)\left(\frac{r_{\rm out}}{r_{\rm out} - r_{\rm in}}\right) \tag{A3}$$

$$r = \sqrt{\Delta x^2 + \Delta y^2} \quad \text{(circular} - \text{centric distance)} \tag{A4}$$

$$\tanh\left(r_{\rm in}, r_{\rm out}, \theta_{\rm incl}, \theta^{\rm sky}_{\rm P.A.}; r\right) \equiv 0.5 \times \left(\tanh\left[B\left(\frac{r}{r_{\rm out}} - 1\right) + 2\right] + 1\right). \tag{A5}$$

APPENDIX B

HYPERBOLIC TANGENT TRUNCATION FUNCTION

The hyperbolic tangent truncation function ($\tanh(x_0, y_0; r_{\rm break}, r_{\rm soft}, q, \theta_{\rm P.A.})$) (see Section 5) is very similar to the coordinate rotation formulation in Appendix A, except for different constants that define the flux ratio at the truncation radii: at $r = r_{\rm break}$ the flux is 99% of the untruncated model profile, whereas at $r = r_{\rm soft}$ the flux is 1%. With this definition, Equation (B2) is the truncation function:

$$B = 2.65 - 4.98\left(\frac{r_{\rm break}}{r_{\rm break} - r_{\rm soft}}\right) \tag{B1}$$

$$\tanh(x_0, y_0; r_{\rm break}, r_{\rm soft}, q, \theta_{\rm P.A.}) \equiv 0.5 \times \left(\tanh\left[(2 - B)\frac{r}{r_{\rm break}} + B\right] + 1\right). \tag{B2}$$

Note that the radius r is a generalized radius (as opposed to a circular-centric distance), i.e., one that is perturbed by C_0, bending modes, or Fourier modes, of the truncation function. When the softening length ($\Delta r_{\rm soft}$) is used as a free parameter, it is defined as $\Delta r_{\rm soft} = r_{\rm break} - r_{\rm soft}$.

REFERENCES

Abraham, R. G., Valdes, F., Yee, H. K. C., & van den Bergh, S. 1994, ApJ, 432, 75
Abraham, R. G., van den Bergh, S., & Nair, P. 2003, ApJ, 588, 218
Andredakis, Y. C., & Sanders, R. H. 1994, MNRAS, 267, 283
Athanassoula, E., Morin, S., Wozniak, H., Puy, D., Pierce, M. J., Lombard, J., & Bosma, A. 1990, MNRAS, 245, 130
Barden, M., et al. 2005, ApJ, 635, 959
Beckwith, S. V. W., et al. 2006, AJ, 132, 1729
Bedregal, A. G., Aragón-Salamanca, A., & Merrifield, M. R. 2006, MNRAS, 373, 1125
Bell, E. F., et al. 2004a, ApJ, 600, L11
Bell, E. F., et al. 2004b, ApJ, 608, 752
Bender, R., Burstein, D., & Faber, S. M. 1992, ApJ, 399, 462
Bertin, E., & Arnouts, S. 1996, A&AS, 117, 393
Binney, J., & Tremaine, S. 1987, Galactic Dynamics (Princeton, NJ: Princeton Univ. Press)
Boroson, T. 1981, ApJS, 46, 177
Burstein, D. 1979, ApJ, 234, 435
Byun, Y. I., & Freeman, K. C. 1995, ApJ, 448, 563
Conselice, C. J., Bershady, M. A., Dickinson, M., & Papovich, C. 2003, AJ, 126, 1183
Conselice, C. J., Bershady, M. A., & Jangren, A. 2000, ApJ, 529, 886
Cote, P., et al. 2006, ApJ, 165, 57
Cote, P., et al. 2007, ApJ, 671, 1456
de Jong, R. S. 1996, A&AS, 118, 557
de Souza, R. E., Gadotti, D. A., & dos Anjos, S. 2004, ApJS, 153, 411
de Vaucouleurs, G. 1948, Ann. d'Astrophys., 11, 247
Djorgovski, S., & Davis, M. 1987, ApJ, 313, 59
Dressler, A. 1980, ApJ, 236, 351
Dressler, A., Lynden Bell, D., Burstein, D., Davies, R. L., Faber, S. M., Terlevich, R., & Wegner, G. 1987, ApJ, 313, 42
Elson, R. A. W. 1999, in 10th Canary Islands Winter School of Astrophysics, Globular Clusters, ed. C. Martínez Roger, I. Perez Fournón, & F. Sánchez (Cambridge: Cambridge Univ. Press) 209
Faber, S. M., et al. 1997, AJ, 114, 1771
Faber, S. M., et al. 2007, ApJ, 665, 265
Ferrarese, L., Cote, P., Blakeslee, J. P., Mei, S., Merritt, D., & West, M. J. 2006a, arXiv:astro-ph/0612139
Ferrarese, L., & Merritt, D. 2000, ApJ, 539, L9
Ferrarese, L., et al. 2006b, ApJS, 164, 334
Freeman, K. C. 1970, ApJ, 160, 811
Gadotti, D. A. 2008, MNRAS, 384, 420
Gebhardt, K., et al. 2000, ApJ, 539, L13
Hathi, N. P., Ferreras, I., Pasquali, A., Malhotra, S., Rhoads, J. E., Pirzkal, N., Windhorst, R. A., & Xu, C. 2009, ApJ, 690, 1866
Häussler, B., et al. 2007, ApJS, 172, 615
Heymans, C., et al. 2006, MNRAS, 371, L60
Heymans, C., et al. 2008, MNRAS, 385, 1431
Hinz, J. L., Rieke, G. H., & Caldwell, N. 2003, AJ, 126, 2622
Hopkins, P. F., Cox, T. J., Dutta, S. N., Hernquist, L., Kormendy, J., & Lauer, T. R. 2009, ApJS, 181, 135
Hopkins, P. F., Hernquist, L., Cox, T. J., Dutta, S. N., & Rothberg, B. 2008, ApJ, 679, 156
Hutchings, J. B., Crampton, D., & Campbell, B. 1984, ApJ, 280, 41
Jahnke, K., et al. 2004, ApJ, 614, 568
Kent, S. M. 1985, ApJS, 59, 115
Kim, M., Ho, L. C., Peng, C. Y., Barth, A. J., & Im, M. 2008a, ApJS, 179, 283
Kim, M., Ho, L. C., Peng, C. Y., Barth, A. J., Im, M., Martini, P., & Nelson, C. H. 2008b, ApJ, 687, 767
Kormendy, J. 1977, ApJ, 217, 406
Kormendy, J. 1985, ApJ, 292, L9
Kormendy, J. 1987, in Nearly Normal Galaxies from the Planck Time to the Present, 163
Kormendy, J. 1999, in ASP Conf. Ser. 182, Galaxy Dynamics: A Rutgers Symp., ed. D. R. Merritt, M. Valluri, & J. A. Sellwood (San Francisco, CA: ASP), 124
Kormendy, J., & Bender, R. 2009, ApJ, 691, L142
Kormendy, J., & Richstone, D. 1995, ARA&A, 33, 581
Kormendy, J., et al. 2009, ApJS, 182, 216
Krist, J. E., & Hook, R. N. 1997, in The 1997 HST Calibration Workshop with a New Generation of Instruments, ed. S. Casertano, R. Jedrzejewski, T. Keyes, & M. Stevens (Baltimore, MD: STScI), 192
Lauer, T. R., et al. 1995, AJ, 110, 2622
Lauer, T. R., et al. 2007, ApJ, 664, 226
Laurikainen, E., et al. 2004, MNRAS, 355, 1251
Lilly, S., et al. 1998, ApJ, 500, 75
Lisker, T. 2008, ApJS, 179, 319
Lotz, J. M., Primack, J., & Madau, P. 2004, AJ, 128, 163
Lotz, J. M., et al. 2008, ApJ, 672, 177
MacArthur, L. A., Courteau, S., & Holtzman, J. A. 2003, ApJ, 582, 689
Marleau, F. R., & Simard, L. 1998, ApJ, 507, 585
Massey, R., Refregier, A., Conselice, C. J., David, J., & Bacon, J. 2004, MNRAS, 348, 214
McLeod, K. K., & Rieke, G. H. 1994, ApJ, 431, 137
McLure, R. J., Dunlop, J. S., & Kukula, M. J. 2000, MNRAS, 318, 693
Moffat, A. F. J. 1969, A&A, 3, 455
Moriondo, G., Giovanardi, C., & Hunt, L. K. 1998, A&AS, 130, 81
Pence, W. 1999, in ASP Conf. Ser. 172, Astronomical Data Analysis Software and Systems VIII, ed. D. M. Mehringer, R. L. Plante, & D. A. Roberts (San Francisco, CA: ASP), 487
Peng, C. Y., Ho, L. C., Impey, C. D., & Rix, H.-W. 2002, AJ, 124, 266
Peng, C. Y., Impey, C. D., Ho, L. C., Barton, E. J., & Rix, H.-W. 2006a, ApJ, 640, 114
Peng, C. Y., Impey, C. D., Rix, H.-W., Kochanek, C. S., Keeton, C. R., Falco, E. E., Lehár, J., & McLeod, B. A. 2006b, ApJ, 649, 616
Press, W. H., Teukolsky, S. A., Vetterling, W. T., & Flannery, B. P. 1992, Numerical Recipes in C. The Art of Scientific Computing (2nd ed.; Cambridge: Cambridge Univ. Press)
Ratnatunga, K. U., Griffiths, R. E., & Ostrander, E. J. 1999, AJ, 118, 86
Ravindranath, S., Ho, L. C., & Filippenko, A. V. 2002, ApJ, 566, 801
Ravindranath, S., et al. 2004, ApJ, 604, L9
Refregier, A. 2003, MNRAS, 338, 35
Rix, H.-W., Falco, E. E., Impey, C., Kochanek, C., Lehár, J., McLeod, B., Muñoz, J., & Peng, C. 2001, in ASP Conf. Ser. 237, Gravitational Lensing: Recent Progress and Future Goals, ed. T. G. Brainerd & C. S. Kochanek (San Francisco, CA: ASP), 169
Rix, H.-W., et al. 2004, ApJS, 152, 163
Rudnick, G., & Rix, H.-W. 1998, AJ, 116, 1163
Sánchez, S. F., et al. 2004, ApJ, 614, 586
Shaw, M. A., & Gilmore, G. 1989, MNRAS, 237, 903
Simard, L. 1998, in ASP Conf. Ser. 145, Astronomical Data Analysis Software and Systems VII, ed. R. Albrecht, R. N. Hook, & H. A. Bushouse (San Francisco, CA: ASP), 108
Simard, L., et al. 2002, ApJS, 142, 1
Stetson, P. B. 1987, PASP, 99, 191
Tully, R. B., & Fisher, J. R. 1977, A&A, 54, 661
van der Kruit, P. C., & Searle, L. 1981, A&A, 95, 105
Wadadekar, Y., Robbason, B., & Kembhavi, A. 1999, AJ, 117, 1219
Williams, R. E., et al. 1996, AJ, 112, 1335